2019, Sept. 20.

Rh-induced Support Transformation Phenomena in Titania and Titanate Catalysts and Its Influences on the Catalytic Activity

János Kiss[1,2*], András Sápi[1], Mariann Tóth[1], Ákos Kukovecz[1], Zoltán Kónya[1,2]

[1]*University of Szeged, Interdisciplinary Excellence Centre, Department of Applied and Environmental Chemistry, H-6720, Rerrich Béla tér 1, Szeged, Hungary*
[2]*MTA-SZTE Reaction Kinetics and Surface Chemistry Research Group, Rerrich Béla tér 1, Szeged, H-6720 Hungary*

[*]Corresponding author: jkiss@chem.u-szeged.hu

Abstract: Rh is one of the most effective metals in several technologically important reactions, mainly in the hydrogenation of CO_2, CO, in the CO+H_2O reaction, and methane and ethanol transformations. Titania and titanates are the most studied supports for Rh nanoparicles. It is demonstrated in present study that the nature of the support has a marked influence on the specific activity. We pay distinguished attention not only to the electronic interaction between Rh metal and titania and titanate support but also the Rh-induced phase transitions of one-dimensional titanate nanostructures. The structure and morphology of pristine and Rh-decorated nanowires (TiONW) and nanotubes (TiONT) were studied by HRTEM and XRD. The surface chemical composition was studied by XPS, FT infrared, and Raman-spectroscopy. For comparison, the morphology of TiO_2 was also tested. Support transformation phenomena were observed in Rh-loaded titanates. Rh decorated nanowire transform into the β-TiO_2 structure, where their pristine counterparts' recrystallize into anatase. The formation of anatase was dominant during the thermal annealing process in both acid treated and Rh decorated nanotubes. We pointed out that the phase transformations have influences on conversion and selectivity of the above-mentioned reactions. The following initial activity order was found in the CO_2 + H_2, CO + H_2O and C_2H_5OH

[S1] megjegyzést írt: besides cracking and other C-C cleavage reactions

decomposition reactions: Rh/TiO_2 (Degussa P25) > Rh/TiONW > TiONT. In certain cases, the turnover frequencies were almost the same. It is remarkable that the hydrogen selectivity in ethanol decomposition was two times higher on nanowire and nanotube supported Rh catalysts than on Rh/TiO_2.

[S2] megjegyzést írt: Ide egy mondatban jo lenne megirni hogy mi az oka ennek. Pl. which can be attributed to the special TiO2 phase transition-based Rh/TiOx complex interphase formation

Keywords: Rh catalyst, titanate nanowires, titanate nanotubes, phase transformation, CO_2 hydrogenation, WGS reaction, ethanol decomposition

1. Introduction

Heterogeneous catalysts are a key component in 21st century technology. Not only ~~are~~ most bulk and fine chemicals produced using heterogeneously catalyzed reaction steps, but suitable catalysts may also be the key ingredients in future energy production, energy storage and solving environmental problems [1,2]. CO_2 is a problem and there is a need for chemical activation of such stable molecules. Catalytic CO_2 hydrogenation not only reduce the anthropogenic emission of CO_2 but also produces value added liquid fuels and feedstock chemicals. CO_2 conversion using H_2 produced from electrolysis of water generated by wind or solar energy produces carbon monoxide (CO), methane (CH_4) and methanol (CH_3OH) etc. is considered to be promising approach to reduce CO_2 level [3-10]. Because of the chemical inertness of CO_2 and thermodynamic stability, the chemical activation of CO_2 is a rather popular buzzword nowadays in catalysis and surface science, the efficient and selective CO_2 conversion remains a challenge [11-14]. The water gas shift reaction (WGSR) [15, 16] and the ethanol (methanol) decomposition and ethanol steam reforming (ESR) serve hydrogen for the energy source [17-19].

The hydrogenation of CO_2, the WGSR and the ethanol transformation reaction including ESR were studied extensively on different noble metals such as~~, among them~~ Rh, which has been shown to be one of the most effective metal. It was found that the support exerted a marked influence on the specific activity of the Rh. The most effective support was TiO_2 and the less effective one was SiO_2. For example in CO_2 hydrogenation, using TiO_2 support, mainly methane was formed with high conversion and with high selectivity, in some cases higher than 95% [20-22]. The catalytic reactions have been investigated as a function of the electric properties of the TiO_2 support induced by doping TiO_2 with cations lower- and higher-valencies [23, 24]. It was

demonstrated that variation of the electric conductivity of TiO_2 influences the catalytic properties of Rh.

A broad literature coverage and excellent reviews are available on TiO_2 and TiO_2 nanostructures [25–27], perovskites [28] and anodically oxidized vertically oriented free standing TiO_2 nanotube arrays [29, 30]. In the last twenty years, several studies with increasing number have been published on the properties of polytitanate –based layered nanostructures even though titanate nanowires and nanotubes. Various tubular metal oxides have been developed recently and are of interest because they are expected to exhibit novel physical and chemical properties. One-dimensional TiO_2 related nanomaterials with high morphological specificity, such as nanotubes and nanowires have attracted considerable attention due to their interesting chemical and physicochemical properties [31-34]. On the basis of the pioneering work of Kasuga et al.,[35] research efforts on titanates were at first concentrated on the hydrothermal synthesis and structure elucidation of titanate nanotubes. Recently, hydrothermal conversion of self-assembled titanate nanotubes (TiONT) into nanowires (TiONW) in a revolving autoclave was achieved in our laboratory [36, 37]. Titanate nanostructures are of great interest for catalytic applications, since their high surface area and cation exchange capacity provides the possibility of achieving a high metal (e.g. Co, Cu, Ni, Ag and Au) dispersion [34, 38-41]. Bavykin and Walsh reported an excellent review about the preparation, characterization and application of titanate and titanate nanotubes [42]. Recently a comprehensive review was published of the one dimensional titanate nanomaterials [43]. Atomic scale characterization and surface chemistry of metal modified titanate nanotubes and nanowires.

Recently it was found that titanate nanostructures (nanowires and nanotubes) could stabilize gold in a high-dispersed form [41, 44-46]. Up to now some important titanate supported gold catalytic reactions were discovered. Gold-containing titanate nanotubes were found to display higher activity than the Degussa P-25 catalyst in the photo-oxidation of acetaldehyde [47], in the photocatalytic degradation of formic acid [48], in the low-temperature water-gas shift reaction [49] and in CO oxidation [46, 50, 51] and it is active catalysts in thermal induced CO_2 hydrogenation [52]. Very recently, it was turned out that gold nanoparticles supported on titanate nanowires efficient in the UV photo-induced reaction of methane and in CO_2 hydrogenation [13, 14]. There are some examples that other noble metals supported on titanate nanostructures also perform remarkably in catalytic processes.

As the Rh on titania-based support performs excellent catalytic activity in many reactions, it is desirable to summarize the Rh-titanate interaction and review the effect of titante nanostructures on above-mentioned reactions. In the first part, we are discussing the Rh-induced transformation of titanates (wires and tubes) and the surface characterization of Rh on titanates. In the second part, we are studying mainly the $CO_2 + H_2$ reaction on different titanates, and then we focus to the water gas shift reaction and less extent for comparison to the steam reforming of ethanol.

2. Experimental

Titanate nanowires (TiONW) and nanotubes (TiONT) were prepared by mixing 2 g of anatase into 140 cm^3 10 M aqueous NaOH solution until a white suspension was obtained, aging the suspension in a closed, cylindrical, Teflon-lined autoclave at 400 K for 1-72 h (depending on the desired product) while rotating the whole autoclave intensively at 0-60 rpm around its short axis, and finally washing the product with deionized water and neutralizing with 0.1 M HCl acid solution to reach pH=7. At this point, the titanate nanostructure slurry was filtered and dried in air at 353 K [35, 36, 53]. Acid washing is a standard method in titanate nanotube and nanowire synthesis. It is used to exchange as much Na^+ ions in the structure to protons as possible. The resulting material is generally referred to as "H-form" titanate.

Titanate nanotubes are open-ended hollow tubular objects measuring 7-10 nm in outer diameter and 50-170 nm in length. They feature a characteristic spiral cross section composed of 4-6 wall layers. The typical diameter of their inner channel is 5 nm [35, 43, 53]. Titanate nanowires represent the thermodynamically most stable form of sodium trititanate under the alkaline hydrothermal conditions applied in titanate nanotube synthesis as well. (Note that the post-synthetic neutralization step converts the original $Na_2Ti_3O_7$ into its hydrogen form without affecting the nanowire morphology.) Their diameter is 45-110 nm and their length is between 1.8 and 5 μm [36, 43]. The specific surface area of titanate nanotubes is rather large (~185 m^2g^{-1}) due to their readily accessible inner channel surface, whereas that of titanate nanowires is ~20-40 m^2g^{-1}.

Rh/titanate nanocomposites with different Rh concentrations were produced by impregnating titanate nanowires and nanotubes with mixtures of calculated volumes of $RhCl_3x3$ H_2O (Johnson Matthey) solutions to yield 1 and 2.5 wt% metal content. The impregnated powders

were dried in air at 383 K for 3 h. The final pre-treatment was at 473-573 K in hydrogen atmosphere [33, 43, 54-58]. Both acid-treated (H-titantes) and Rh decorated nanotubes and nanowires underwent a thermal annealing process at elevated temperature (473–873 K) for 1 hour. Samples were removed after each thermal operation for further characterization.

XP spectra were taken with a SPECS instrument equipped with a PHOIBOS 150 MCD 9 hemispherical analyzer. The analyzer was operated in the FAT mode with 20 eV pass energy. The Al K_α radiation ($h\nu$=1486.6 eV) of a dual anode X-ray gun was used as an excitation source. The gun was operated at the power of 210 W (14 kV, 15 mA). The energy step was 25 meV, electrons were collected for 100 ms in one channel. Typically five scans were summed to get a single high-resolution spectrum. The Ti $2p_{3/2}$ maximum (458.9 eV) was used as binding energy reference. The same data were obtained when C 1s (adventitious carbon at 285.1 eV), or O 1s lattice oxygen (530.4 eV) was used as reference. Sample preparation (oxidation-reduction) for XPS measurements were carried out in situ in preparation chamber. The sample preparation chamber was directly connected to the measuring chamber to avoid the contamination of samples between the steps. Self-supporting pellets were used in XPS measurements. For spectrum acquisition and evaluation both manufacturer's (SpecsLab2) and commercial (CasaXPS, Origin) software packages were used.

IR studies in reflection mode were performed in a high vacuum system. The samples were pressed onto a tantalum mesh. The mesh was fixed to the bottom of a conventional UHV sample manipulator. It was resistively heated and the temperature of the sample was measured with a NiCr-Ni thermocouple spot welded directly to the mesh. IR spectra were recorded with a Genesis (Mattson) FTIR spectrometer. DRIFT spectra were recorded with a BioRad FTS-135 FT-IR spectrometer equipped with a diffuse reflectance attachment (Thermo Electron Corporation) with BaF_2 windows. Typically 256 scans were registered at a spectral resolution of 2 cm^{-1}. All spectra were recorded at 293 K. The optical path was purged with CO_2- and H_2O-free air generated by a Whatman purge gas generator. The reference sample was KBr, treated in oxygen at 500 K for 20 min, then in He atmosphere for 40 min. He 4.6 gas was used for inner purging in each experiment. The residual water contamination in He was frozen out with liquid nitrogen via in a 1/8” diameter copper tube trap.

Raman spectra of slightly pressed powder samples were measured in 180° backscattered geometry at 785 nm laser excitation (incident laser power 460 mW) using an Ocean Optics

QE65000 spectrometer coupled to an Ocean Optics Raman probe. Scans were integrated at 4 cm^{-1} resolutions until the desired signal-to-noise ratio of 1000 or better was achieved (typically 30 seconds).

Temperature programmed desorption and simultaneous thermogravimetric measurements were carried out in a Netzsch STA 409 PC microbalance connected to a Pfeiffer QMS 200 mass spectrometer system. The changes in the mass spectrometer signal intensity of water (18 amu) were monitored during the measurements. The samples were heated at a heating rate of 10 K/min from 300 K up to 878 K in He 4.6 stream (40 ml/min).

The morphology of the pristine and modified titanate nanostructures was characterized by transmission electron microscopy (FEI Tecnai G^2 20 X-Twin; 200 kV operation voltage, x180000 magnification, 125 pm/pixel resolution). The Rh particle size distribution was determined by image analysis of the TEM pictures using the ImageJ software. At least five representative images of equal magnification, taken at different spots of the TEM grid were first subjected to rolling ball background subtraction and contrast enhancement, then the diameter of the metal nanoparticles in the image was manually measured against the calibrated TEM scalebar. Each diameter distribution histogram was constructed from 200 individual nanoparticle diameters. X-ray powder diffractometry (Rigaku MiniFlexII; utilizing a CuK_α x-ray source) and electron diffraction technique (integrated into TEM) were used for crystal structure and crystallinity determinations.

The catalytic set up was described in a more detail previously [20, 52, 56, 57]. The reaction were carried out in a fixed bed continuous-flow reactor. The amount of catalysts used usually about 0.1 g. The dead volume of the reactor was filled with quartz chips. The flow rate was usually 50 ml/min.Analysis of the product gases was performed with a Chrompack 9001 gas chromatograph using Porapak QS column. The products were detected simultaneously by TC and FI detectors.

3. Results and Discussion

3.1. Phase transformation of heat-treated pristine (H-titante) and Rh-decorated titanates

Rh induced phase transformation of titanates

Raman spectra of pristine and heat treated titanate nanotubes and nanowires are presented in Fig. 1A and 2B together with the spectrum of a reference anatase sample. The spectra of as-synthesized nanostructures match previous trititanate results where peaks in the 400-1000 cm^{-1} region were assigned to Ti–O–Ti stretching vibrations [59, 60]. The thermal behavior of the

samples basically confirms our independent infrared spectroscopic, thermogravimetric and XRD measurements as well as literature findings [61] insofar as the trititanate structure appears to be deconstructed at approx. 573 K. Annealing at higher temperatures initiates the trititanate to anatase conversion process which is concluded at 873 K as indicated by the good match between the 873 K spectrum and the reference anatase curve. Peaks at 393, 514 and 636 cm^{-1} are assigned to the B_{1g}, A_{1g} and E_{2g} modes of anatase, respectively [59].

A characteristic difference between the behavior of titanate nanotubes and nanowires is that in heat treated nanotubes the E_{2g} mode is found at exactly the anatase position (636 cm^{-1}) from 573 K onwards, whereas in nanowires this mode experiences a gradual red shift from 648 cm^{-1} at 573 K to 636 cm^{-1} at 873 K. A similar effect was observed by Du et al. [62] and Scepanovic et al. [63] in their in situ temperature-dependent Raman studies of nanocrystalline anatase. They argued that defects and nonstoichiometric composition could have a pronounced effect on the position of the soft E_g modes. Adopting this argument to one-dimensional trititanates suggests that the thin and hollow structure of nanotubes is more easily converted to defect-free anatase than the bulky nanowires. This interpretation is further supported by our XRD and ED measurements.

Figures 4C and 4D present the Raman spectra of Rh loaded titanate nanotubes and nanowires, respectively, as a function of heat treatment temperature. The final product of the transformation of Rh loaded nanotubes features the characteristic anatase peaks at 393, 514 and 636 cm^{-1} assigned to the B_{1g}, A_{1g} and E_{2g} modes, respectively. On the other hand, the Raman spectrum of the recrystallized Rh containing titanate nanowires lacks these anatase signals. The spectral series in Figure 4D illustrates the temperature evolution of a shoulder at 364 cm^{-1}, an envelope of overlapping peaks centered at 412 cm^{-1}, a broad peak centered at 644 cm^{-1} and a very broad peak at 854 cm^{-1}. A similar Raman spectrum was recently identified as that of a β-TiO_2 phase by Wang et al. [64]. Therefore, we conclude that (i) the 873 K heat treatment of Rh loaded titanate nanotubes and nanowires yields products of different phase structure, (ii) Rh loaded titanate nanotubes transform into anatase under the studied experimental conditions and (iii) the spectral features of the transformation product of Rh loaded titanate nanowires can be adequately explained by assuming that this product exhibits the β-TiO_2 structure.

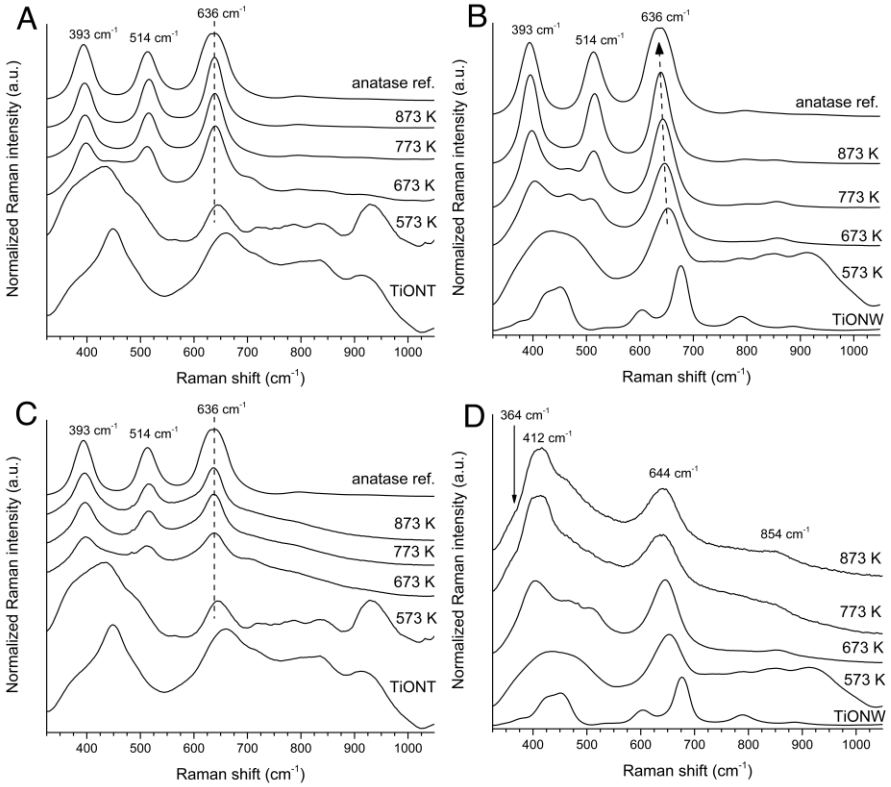

Figure 1. Normalized Raman spectra of the thermal behavior of trititanate nanotubes (A) and nanowires (B). The spectra of as-synthesized samples are depicted at the bottom and the spectrum of a commercial anatase reference sample is shown at the top of each graph. Graphs C and D illustrate the thermal behavior of Rh loaded trititanate nanotubes and nanowires, respectively. Reproduced from Ref. [58].

The crystal structure of the pristine nanowires is a mixture of different titanate forms, mostly β-TiO_2 and $H_xNa_{(2-x)}Ti_3O_7$ as shown in XRD patterns (Figure 2A). The β-TiO_2 phase was identified on the basis of its reflections with Miller indices of (200), (110), (002) (111), (003), (020), (022), (71$\underline{1}$), (313), (023) and (712) at 15.4°, 24.9°, 28.6°, 29.4°, 43.5°, 48.5°, 57.3°, 58.3°,

61.7°, 68.2° and 76.8°, respectively. The $H_xNa_{(2-x)}Ti_3O_7$ phase was identified on the basis of its reflections with Miller indices of (001), (101), (011), (300), (203) and (401) found at 10.5°, 15.8°, 25.7°, 29.9°, 34.2° and 43.9°, respectively. Acidic treatment also resulted in crystallinity degradation. The crystal transformation is continuous during the thermal annealing process. XRD as well as ED patterns recorded from a sample annealed at 473 K and 573 K indicated the collapse of the layered structure and the appearance of an anatase phase with low crystallinity. At higher temperature the formation of the anatase phase becomes dominant as demonstrated by the electron diffraction patterns (Figure 2A) as well as by the appearance of the characteristic anatase reflections (101), (004), (200), (105), (211) and (204) at 25.3°, 37.8°, 48.1°, 53.9°, 55.1° and 62.4°. The process is accompanied by the loss of peak intensities at positions corresponding to the titanate interlayer distance (~10°) β-titanate structural reflections (101) at 15.8° and (300) at 29.9°.

The nanowires preserve the wire-like morphology during the heat treatment up to 873 K. However, more and more textural discontinuities can be observed at higher temperatures. The holey structure can be attributed to the continuous transformation of protonated titanate nanostructures to TiO_2 (anatase) followed by water formation and release from the structure. This processes resulted in the rearrangement of the formed anatase crystals and the appearance of unfilled spaces in the structure of the whole nanowire (Fig. 2B).

(A)

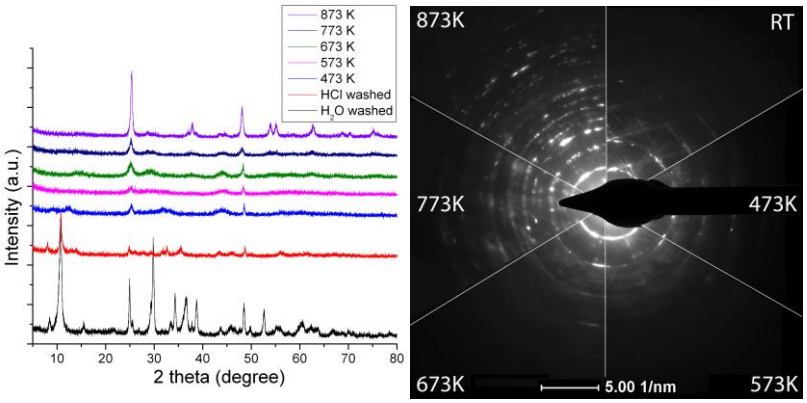

(B)

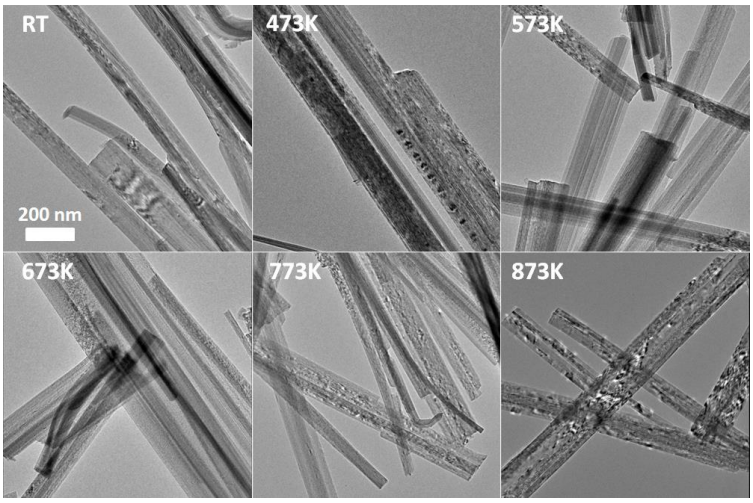

Figure 2. (A) XRD and ED of protonated titanate nanowires treated at different temperatures. (B) TEM images of nanowires treated at different temperatures. Reproduced from Ref. [58].

As XRD and ED patterns show (Fig. 3A), the acidic treatment resulted in a degradation of the initial crystal structure of titanate nanotubes, which manifested in the disappearance of the reflection belonging to the tubular interlayer distance ($2\Theta = \sim 10°$). The protonation also induced the transformation of the titanate nanostructure to anatase form. Thermal treatment below 673 K had no significant effect on the crystal structure; however, at elevated temperature the anatase formation became relevant as evidenced by the appearance of the anatase reflections discussed in detail above (Fig. 3A). Reflections of higher intensity and lower half-width indicated the improvement of anatase crystallinity with increasing temperature as electron diffraction patterns also show in Fig. 3A.

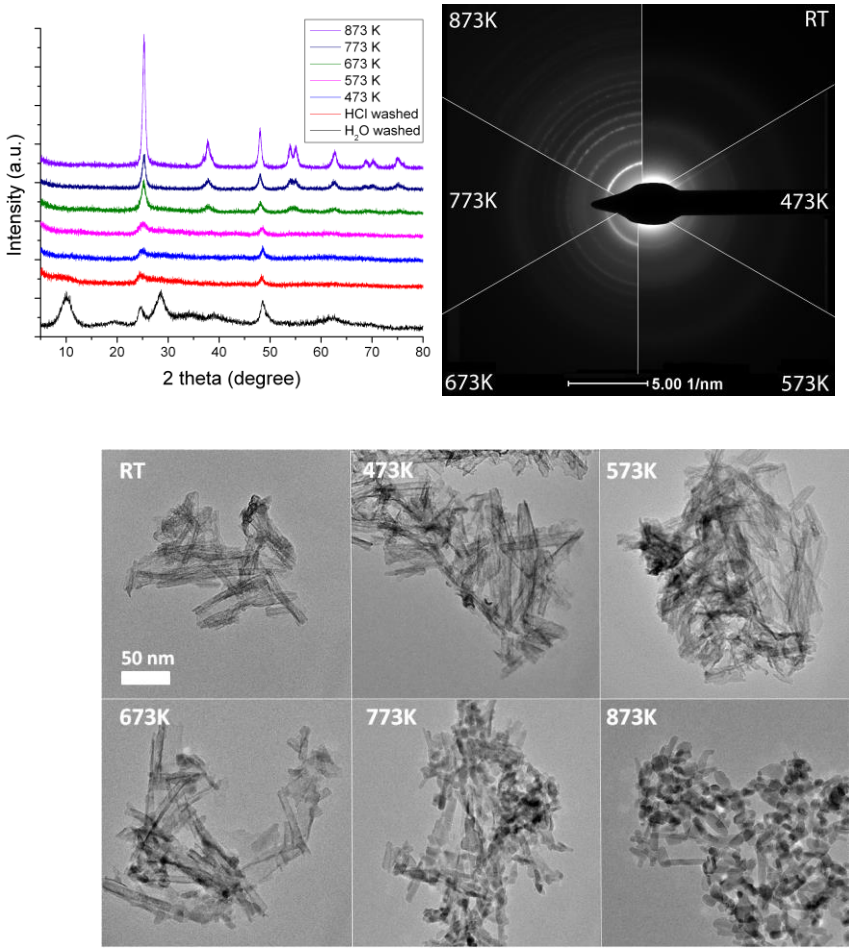

Figure 3. (A) XRD of protonated titanate nanotubes thermally treated at different temperatures. (B) TEM images of nanotubes treated at different temperatures. Reproduced from Ref. [58].

TEM images in Figure 3B demonstrate the tubular morphology of the as-synthesized titanate nanotubes with a diameter of ~7 nm and length up to 80 nm. The acidic washing process resulted in a mild destruction of the inner and outer walls of the nanotubes (not shown here). In correlation with the XRD results, no morphological degradation after heat treatment up to 573 K

could be observed. At higher temperature, the tubular structure started to collapse and transform into rod-like nanostructures. At 873 K the tubular morphology totally collapsed, that resulted in short nanorods and TiO_2 nanoparticles with an average size of ~ 10 nm.

The phase transformation during heat treatment accompanies with structural water loss as was investigated and discussed previously [31, 36, 37, 42, 43, 58]. The sources of water formation are the adsorbed water (or lattice water), and the surface reaction of surface OH groups and hydrogen from the recrystallization process. We should mention that a slower thermal release of water moieties from TiONT compared to TiONW, in harmony with the literature data [43, 58], may have its origin in the condensation of water in TiONT channels. These reactions could significantly increase the number of defects in nanowires and nanotubes and may promote the phase transformation of titanates. The heat treatment induces the reduction of Ti^{4+} in titanates to Ti^{3+} and Ti^{2+}, but their detection in the surface layers is not always successful due to the fast oxygen transport from bulk to surface. The reduction degree of these cations with the annealing temperature was followed by treating nanotubes sample *in situ* in inert atmosphere at different temperatures. When the sample was annealed the population of reduced Ti^{3+} atoms increased giving a Ti^{3+}/Ti^{4+} surface atomic ratio of 0.046 and 0.06 at 573 and 773 K, respectively (Table 1).

Table 1. XPS parameters of Ti $2p_{3/2}$ and O 1s derived from spectral fitting. Reproduced from Ref. [43].

Annealing temperature (°C)	Assignment	Binding energy (eV)	FWHM[a] (eV)	Surface atomic ratio Ti^{3+}/Ti^{4+}	Surface atomic ratio O/Ti
110	O 1s	530.8	1.3	0.026	2.48
	Ti^{3+} $2p_{3/2}$	457.5	1.2		
	Ti^{4+} $2p_{3/2}$	459.1	1.2		
200	O 1s	530.8	1.2	0.048	2.17
	Ti^{3+} $2p_{3/2}$	457.8	1.2		
	Ti^{4+} $2p_{3/2}$	459.2	1.1		
300	O 1s	530.8	1.2	0.046	1.96
	Ti^{3+} $2p_{3/2}$	458.1	1.4		
	Ti^{4+} $2p_{3/2}$	459.4	1.1		
400	O 1s	530.9	1.2	0.045	1.89
	Ti^{3+} $2p_{3/2}$	458.1	1.4		
	Ti^{4+} $2p_{3/2}$	459.4	1.1		
500	O 1s	530.8	1.2	0.060	1.97
	Ti^{3+} $2p_{3/2}$	458.1	1.6		
	Ti^{4+} $2p_{3/2}$	459.4	1.1		

[a]Full width at half maximum.

Rh decorated nanowires transform into the β-TiO_2 structure (Fig. 4A) as opposed to the rhodium-free counterparts' recrystallization to anatase. The formation of the β-TiO_2 structure is indicated by the appearance of XRD peaks with Miller indices of (200), (110), (002) (111), (003), (020), (022), (71$\underline{1}$), (313), (023) and (712) at 15.4°, 24.9°, 28.6°, 29.4°, 43.5°, 48.5°, 57.3°, 58.3°, 61.7°, 68.2° and 76.8°, respectively. Full width at half maximum (FWHM) of the dominant reflections attributed to anatase 25.3° (101) and β-TiO_2 24.9° (110) in case of pristine and Rh decorated titanate nanowires, respectively, indicate the degree of crystallinity at various heat treatment temperatures. Up to 673 K the crystallinity of the samples did not improve as indicated by the constant (Rh decorated nanowires) or increasing (pristine nanowires) FWHM values. This moderate crystal amorphization can be assigned to sample drying and structural water loss. The subsequent recrystallization processes resulting in a coherent system of nanoparticles were preferential in the case of pristine nanowires. At higher temperatures fusion of the nanoparticles becomes favorable and this resulted in lower FWHM values.

The formation of anatase dominated the thermal annealing process in both of acid treated and Rh decorated nanotubes (Figure 4B) as indicated by the appearance of anatase reflections (101), (004), (200), (105), (211) and (204) at 25.3°, 37.8°, 48.1°, 53.9°, 55.1° and 62.4°. The FHWM of the most intensive reflection of anatase (101) at 25.3° indicated that the crystal structure is stable below 673 K compared to the nanowire form and started to improve at elevated temperatures in accordance with TEM and XRD results. The decreasing FWHM shows the increasing degree of crystallinity of both the unmodified and Rh decorated titanate nanotubes at elevated temperatures (>573 K).

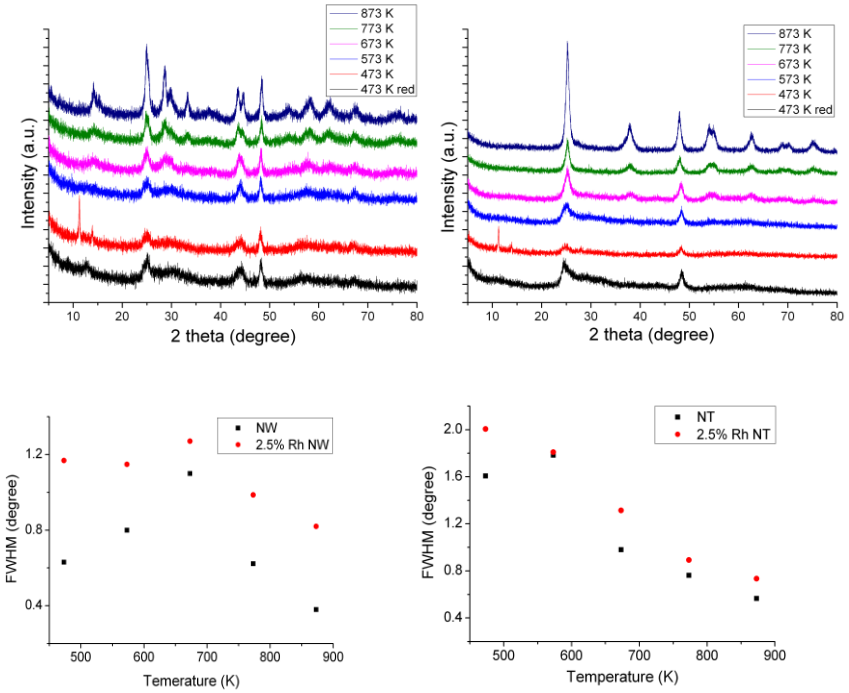

Figure 4. XRD of Rh decorated titanate nanowires (A) and nanotubes (B) heat treated at 473-873 K. The changes of half width of reflection of anatase (101) reflection at 25.3° and the β-TiO_2 (110) reflection at 24.9° during heat treatment are also displayed. Reproduced from Ref. [58].

TEM images of Rh decorated nanowires (Figure 5A) and nanotubes (Fig. 5B) thermally treated at 673 K show the presence of homogeneously dispersed nanoparticles on the surface of titanate nanostructures. The average diameter of nanoparticles is 4.9 ± 1.4 nm and 2.8 ± 0.7 nm in the case of nanowires and nanotubes, respectively, as shown in the corresponding size distributions. The difference in average diameter and distribution broadening can be a result of the difference in the crystal transformation process as discussed above. Moreover, surface diffusion and coalescence kinetics of Rh nanoparticles on the tubular and wire-like forms of titanate nanostructure can be different. No reflections on the XRD patterns of Rh decorated nanostructures (Figure 4) can be assigned to any Rh form due to the relatively low concentration and small size of Rh particles.

Nevertheless, the TEM electron diffraction study of samples heat-treated at 673 K (not shown here) confirmed the presence of metallic Rh in the sample because the characteristic diffraction rings at [hkl] = [111], [200], [220] and [311], corresponding to the d-spacing values of 2.153 Å, 1.885 Å, 1.327 Å and 1.131 Å in the Rh(0) fcc structure, respectively, could be identified.

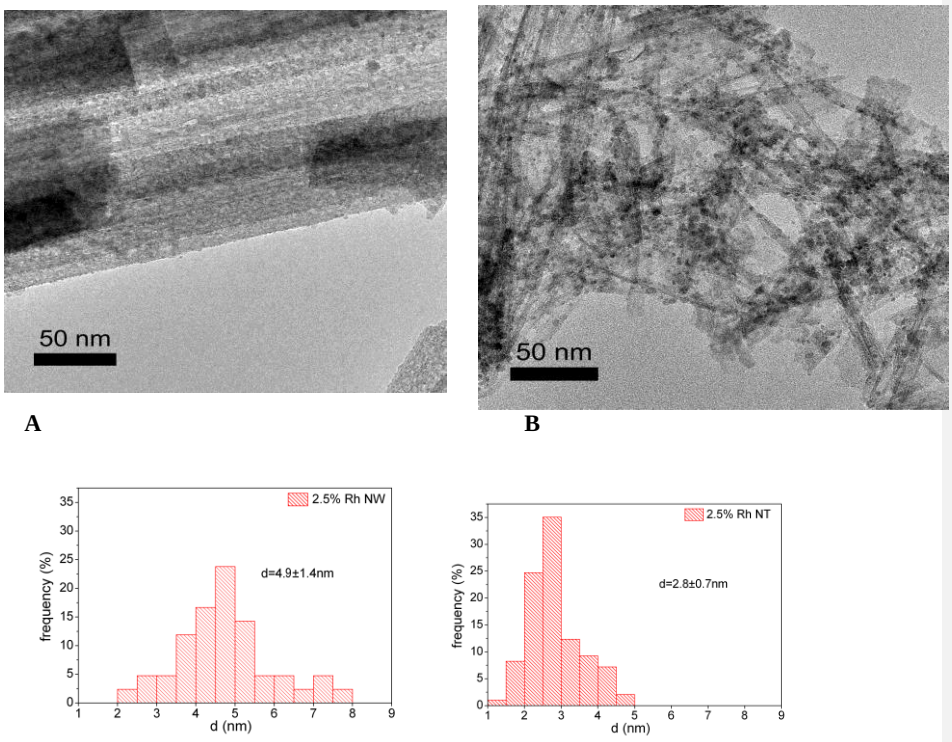

Figure 5. Typical TEM images of 2.5% Rh decorated titanate nanowire (A) and titanate nanotube (B) thermally annealed at 673 K and the corresponding size distribution of Rh nanoparticles. Reproduced from Ref. [58].

It is important to mention that the original low-size distribution is maintained even at relatively high temperatures (reduction temperature of the catalysts: 473-573 K) on both nanowires and nanotubes. Rh clusters of controlled size can be prepared by physical vapor deposition (PVD) [65-67], and using Rh organometallic precursors [68, 69] on TiO_2(110) as well. However, STM

[65, 70], XPS and LEIS [67] experiments revealed that depending on the original cluster size and the evaporation temperature, the agglomeration of Rh nanoparticles can be significant even below 500 K on that surface. The relatively small cluster sizes obtained on titanate nanowires and nanotubes may indicate that the metal diffusion on these nanobjects is limited compared to that of well-ordered titania.

3.2 Morphology and chemical state of Rh nanoparticles on titanates

The morphology of Rh supported on titanate nanowires and nanotubes was investigated by FTIR, employing adsorbed CO as a probe molecule sensitive to the local surface structure. Adsorbed CO exhibits at least three different stretching frequencies belonging to certain adsorption sites of Rh on oxide supports [71-76]. The band at 2070–2030 cm−1 is due to CO being adsorbed linearly to Rh0 (depending on the coverage), the band at ~1855 cm^{-1} represents the bridge bonded CO (Rh_2—CO), and the feature at ~2100 cm−1 and at ~2020 cm−1 corresponds to the symmetric and asymmetric stretching of $Rh^+(CO)_2$ (twin CO). These latter IR signals were detected when the crystallite size was very small [71, 75].

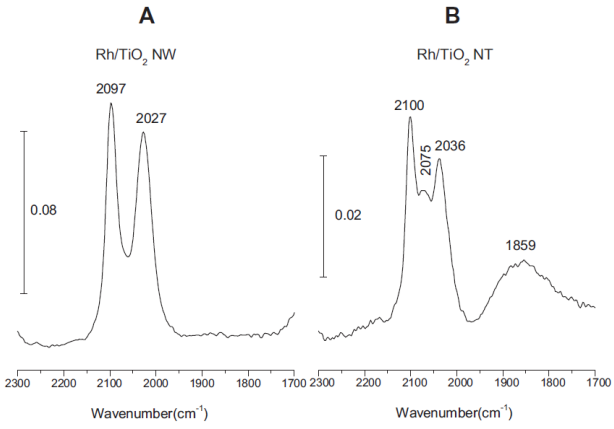

Figure 6. Infrared spectra of adsorbed CO at 300 K. (A) 1% Rh/TiONW, (B) 1% Rh/TiONT

On nanowires, practically the twin form was dominant (2027 and 2097 cm−1), the linear form between these two peaks was much smaller and the bridge form was hardly observable (Fig. 6A).

On nanotubes the linearly adsorbed CO features showed up at 2075 cm−1 between the peaks at 2100 and 2036 cm−1 (twin form) (Fig. 6B). From these IR studies we may conclude that a significant part of Rh exists in small cluster sizes (1-3 nm) probably with Rh^+ oxidation state on both nanowires and tubes.

Fig. 7 shows the binding energies of Rh 3d orbitals in the case nanowires and nanotubes. Photoemission from the Rh 3d peak centered at 309.3 eV at 1 % Rh content and 308.3 eV at 2 % metal content clearly suggest the existence of an oxidation state or morphology different from bulk, as the metallic Rh photoemission for Rh $3d_{5/2}$ is at 307.1 eV. The XP spectra of Rh 3d for 2 % Rh content are presented in Fig. 7. Considering the nearly 2 eV shift relative to metallic Rh, we cannot exclude a certain peak broadening effect due to the width of the nanoparticle distribution. On the other hand the higher binding energy state may correspond to very small clusters stabilized in the structure of nanowires and nanotubes. The binding energy is influenced by the relaxation energy and this "final-state" effect depends on the particle size [77]. This could be explain the observed differences in the intensity ratios of the higher binding energy peaks of samples decorated with smaller (1 % metal loading) and larger (2 % metal loading) Rh nanoparticles.

The stabilization of Rh clusters in small size and the influence of Rh nanoparticles on the transformation of titanate structures can be explained also by the electronic interaction between Rh and titanate, which was observed in several cases between reduced titania and metal including Rh [78-80]. Due to the preparation methods of titanate nanostructures and the mild reduction of Rh/titanates the nanowires and nanotubes may contain significantly more defects than commercially used reduced titania. The presence of a high number of defects and oxygen vacancies in titanate could initiate an increased electron flow between metal and titanates. On the other hand, we cannot exclude the ion exchange between protonated titanates and rhodium, similarly to silver, cobalt and Au on titanates [40, 34, 41]. We may assume that this type of rhodium represents metal (with positive charge) in ion exchange positions.

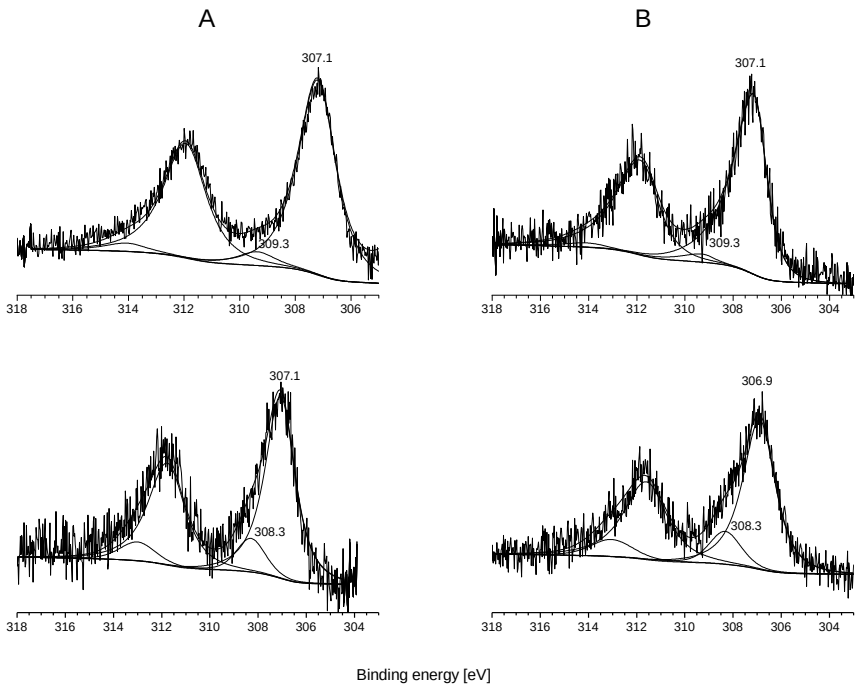

Figure 7. XP spectra of Rh 3d on titanate nanowire (A) and nanotube (B) with 1 % Rh content (upper spectra) and 2% metal content (lower spectra). Reproduced from Ref. [58].

3.3. Effect of co-deposited gold on Rh morphology on titanates

It was demonstrated previously that Rh core–Au shell clusters can be prepared on TiO_2(1 1 0) if Au is postdeposited by physical vapor deposition (PVD) on the oxide surface containing Rh clusters [81, 82]. No separate Au clusters formed in the processat a substrate temperature of 500 K. The existing Rh clusters act as nucleation centers for gold atoms deposited subsequently. The high diffusion rate of Au atoms on the oxide during evaporation probably plays an important role in this process. It was found that the formation of core–shell Rh–Au particles did not depend on the state of reduction of the surface: it proceeded both on unreconstructed TiO_2(1 1 0) and also on the more reduced TiO_2(1 1 0)-(1x2) [83]. The thermodynamic driving force that Au atoms tend to be outside within bimetallic clusters comes from the significantly lower surface free energy of Au compared

to Rh [44]. When the reverse deposition sequence was applied, i.e. Rh was deposited on the $Au/TiO_2(1\ 1\ 0)$ surface, a very efficient place exchange between Rh and Au atoms was observed by LEIS even at room temperature, moving Rh atoms into subsurface regions of bimetallic clusters and the cluster surface remained covered by gold [81]. This indicates that diffusion processes within small metal clusters are rather facile compared to bulk materials.

The surface composition of Au–Rh clusters on titanate nanocomposite was also investigated by LEIS [56]. As was observed in the case of $TiO_2(1\ 1\ 0)$ substrate, with increasing gold content the Rh LEIS intensity decreased dramatically. The most pregnant feature was observed in the 0.5% Au + 0.5% Rh case. On the monometallic systems the gold and rhodium He+ scattering signals appeared at 753 and 707 eV, respectively. On bimetallic nanocomposite, however, only the gold signal showed up (Fig. 8). The rhodium peak was just a bit higher than the noise level. It is very interesting that while the gold content is less (0.5%) in bimetallic system, the LEIS intensity of Au is higher than in the monometallic (1%) case.

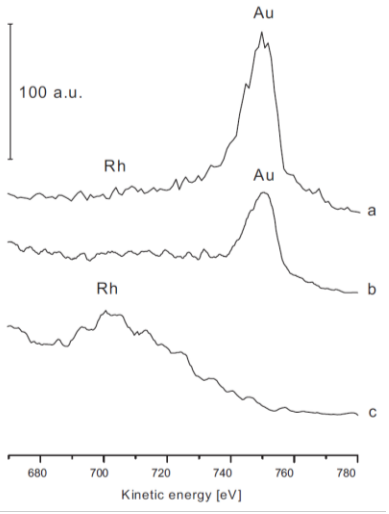

Figure 8. LEIS spectra of 1% Au/TiONW (b), 1% Rh/TiONW (c), 0.5% Au + 0.5% Rh/TiONW (a). Reproduced from Ref. [56].

It is plausible that if the gold completely and uniformly covers the Rh nanoparticles (core-shell structure) then adsorbed CO can not be detected by FTIR. However, relatively strong

CO bands appeared at 300 K at a pressure of 1.3 mbar. In the presence of gold, the peak corresponding to the linear form became stronger at 2070-2071 cm^{-1} and the twin CO stretching frequencies decreased (Fig. 9).

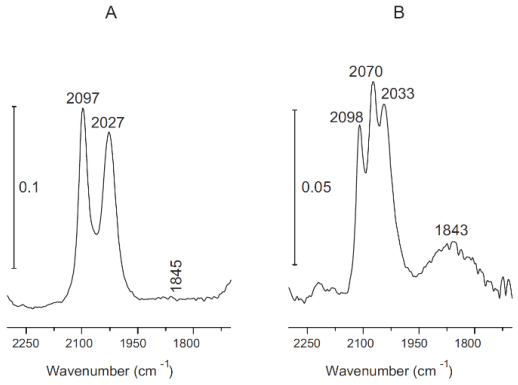

Figure 9. FTIR spectra of adsorbed CO at 300 K: (A) 1% Rh/TiONW and (B) 0.5% Au + 0.5% Rh/TiONW. Reproduced from Ref. [56].

Apparently, there is a contradiction between the results of LEIS and CO adsorption infrared experiments. On the topmost layer there are no Rh atoms (Fig. 9) yet adsorbed CO was detected by FTIR on this surface (Fig. 9B). This discrepancy can be explained by a CO induced surface reconstruction. The adsorption of CO on Au–Rh clusters may promote the diffusion of Rh to the surface of the cluster. Similar phenomena was observed recently in the case of bimetallic Pt–Au clusters on TiO_2(110) [84]. The same effect was also observed on Pd–Au bimetallic model catalysts, synthesized either as thin films on Mo(110) or as nanoparticles on TiO_2 thin film in CO oxidation at elevated (8-16 Torr) CO pressures [85]. Pd preferentially segregates to the surface to form contiguous Pd sites and CO oxidation reactivity is regained. The differences obtained on FTIR spectra between monometallic Rh and bimetallic Au–Rh nanoclusters on titanate nanowire are not surprising. The presence of the core-shell composites and the separate highly dispersed gold clusters may significantly affect the morphology and electronic structure of Rh nanoparticles and therefore, the bonding modes of CO adsorbed on Rh sites as well. The morphology and crystallite size of segregated Rh could be different in the vicinity of Au–Rh core–shell and in the inside of the core-shell structure itself.

In order to get closer to the understanding of CO-induced morphological changes, some low energy ion scattering measurements (LEIS) were carried out before and after CO adsorption on Au–Rh bimetallic clusters supported on titanate nanotubes. In these experiments two compositions were used: 0.25% Au + 0.75% Rh/TiONT and 0.5% Au + 0.5% Rh/TiONT. The results are represented in Fig. 10. In order to avoid or minimize the sputtering effect of the He ions we applied a relatively low ion flux (0.03 $\mu A/cm^2$). At the lower gold content rhodium scattering appeared at 707 eV after hydrogen treatment at 573 K. After CO adsorption at 300 K its intensity increased by about 20% (Fig. 10). The effect of adsorbed CO was more pronounced in the 0.5% Au + 0.5% Rh case. Practically no or very small Rh scattering signal was detected indicating that the gold covered the rhodium particles (Fig. 49B), similarly to the nanowire case (Fig. 45). When CO was added to the bimetallic composite, the rhodium ion scattering signal showed up. These experimental data strongly support the above mentioned phenomena, namely that CO induces a reconstruction of the surface. Rh preferentially segregates to the surface to form Rh–CO bond.

This process may imply the migration of Rh or Au atoms within the clusters or on the surface of the clusters. Considering that Au–Au and Au–Rh bonds are weaker than Rh–Rh bonds, the movement of Au atoms may appear more probable (the shell “opens”), while Rh atoms move less. The influence of CO gas on this possible process is an open question. Though the Au–CO interaction is rather weak compared to the Rh–CO bond, the CO coverage on the Au capping layer is probably significant at the relatively high CO pressure applied. The adsorbed CO layer may decrease the energy of metal-metal bonds both for Au and Rh, leading to an increased diffusion rate. It is also possible that CO, adsorbed in some hollow site of the Au layer, can form some kind of bond with subsurface Rh atoms and this interaction promotes the displacement of Au atoms and the segregation of Rh.

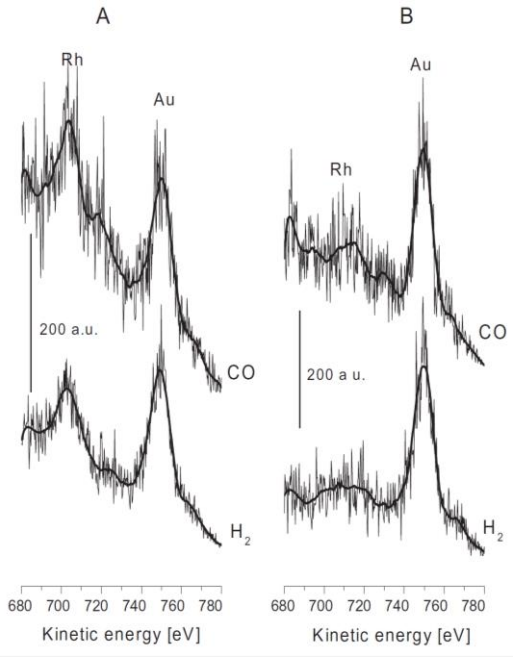

Figure 10. LEIS spectra of 0.25% Au + 0.75% Rh/TiONT (A), 0.5% Au + 0.5% Rh/TiONT (B) before and after CO adsorption at 300 K. The CO pressure was 1.3 mbar. Reproduced from Ref. [56].

Another possible scenario is that there is a continuous thermal fluctuation of metal atoms within the bimetallic clusters independent of the presence of CO, and for short periods Rh atoms can be found on the cluster surface, which are subsequently trapped by CO. The existence of this fluctuation may be possible, since significant movement of metal atoms within small clusters at room temperature was observed in several cases characterized by diffusion coefficients many orders of magnitude higher than the corresponding bulk values [85, 86]. Anyhow, further studies are needed to understand the CO-induced restructuring of Rh–Au clusters in detail.

4. Catalytic reactions on titania and titanate supported Rh catalysts

Nanostructured titanates are characterized by a relatively high specific area, which is typically in the range of 180 to 300 m^2g^{-1} for nanotubes and 20 to 50 m^2g^{-1} for nanowires (nanofibers or nanorods). These values contrast with ~20 m^2g^{-1} for TiO_2 nanotubular arrays produced by electrochemical ways. The range of pore size (from 2 to 10 nm) ranks these materials as mesoporous; such structures are widely used as supports in heterogeneous catalytic processes. The high surface area of the support facilitates high dispersion of the catalyst, while the open mesopores provide efficient transport of both reagents and products [42, 43].

Protonated nanowires and nanotubes have good ion exchange properties. This allows an atomic-scale distribution of metal cations in the titanate lattice. A suitable choice of the ionic form of the metal precursor can significantly help to increase catalyst loading and to maintain high catalysts dispersion. Titanate materials, in which anionic TiO_6 units are countered by other metal cations in a variety of crystal structures are important and employed for instance in catalysis. In addition, the ionic form of metal may increase the catalytic activity in those cases where the redox mechanism is important. In the previous review, a branch of catalytic processes are well-documented [42].

In this paper we focus to the supported Rh because Rh was one of the most effective metals in several technologically important reactions. It was demonstrated that the nature of the support has a marked influence on its specific activity. We pay distinguished attention to not only the electronic interaction between Rh metal and titanate supports, but to the effect of the Rh-induced phase transitions of one-dimensional titanate nanostructures on the catalytic activity. All these information help us to understand and clarify the role of titanate supports in catalytic processes.

4.1 CO_2 hydrogenation on titania and titanate supported Rh

The hydrogenation of CO_2 was studied extensively on titania (TiO_2) supported Rh [21-24, 88-90] and the reaction was also investigated on titante (TiONW and TiONT) supported Rh recently [57, 91]. In all cases, the supported Rh showed excellent catalytic activity. On Table 2. the catalytic activities are summarized obtained on Rh/TiO_2, Rh/TiONW, Rh/TiONT and the effects of co-deposited Au are also displayed and the date are compared with the results obtained on Au/TiO_2, Au/TiONW and Au/TiONT. The catalysts were pretreated the reduction with hydrogen occurred at 573 K. At this temperature the nanotube structure converted partially to anatase, while the Rh induced phase transformation from wire-like structure to β-TiO_2 structure also happens partially. In

the case of Rh/TiONT we have mixed tube-like and nanoanatase composition, in the case Rh/TiONW, wire-like and β-TiO_2 structure exist together. The main product was CH_4 in all cases and small CO formation was detected only on Rh/TiONT. C_2 hydrocarbons were detected only in traces at 493 K. The methane conversions obtained at 493 K are displayed in Fig. 11. H-form titantes were used in CO_2 hydrogenation experiments.

Table 2. Some characteristic data for hydrogenation of carbon dioxide on Rh, Au, Au–Rh bimetallic clusters supported on titanate nanotubes, nanowires and TiO_2. The reaction temperature was 493 K.

Catalyst	Amount of adsorbed H_2 μmol/g	Conversion %		CH_4 formation rate μmol/gs		Turnover number $s^{-1} \times 10^{-3}$	E_a kJ/mol	Σ C μmol/g
		in 5 min	in 80 min	in 5 min	in 80 min	in 80 min	in 80 min	
Rh/TiO_2	7.9	6.9	6.7	4.9	4.4	278	98,3	78.8
Rh/TiONW	7.5	8.9	4.5	6.6	3.2	213	96.5	121.5
Rh/TiONT	4.1	1.4	1	0.8	0.5	61	88.4	132
Au-Rh/TiO_2	2.4	3.3	2.5	2.2	1.5	312	81.3	38.9
Au-Rh/TiONW	5.0	1.5	1.3	1.1	0.9	90	85.3	98.6
Au-Rh/TiONT	2.5	0.4	0.4	0.2	0.1	20	98.8	215.7
Au/TiO_2	0	0.0006	0.0002	$3.7*10^{-4}$	$1*10^{-4}$			17.2
Au/TiONW	0	0.005	0.09	$3.5*10^{-3}$	$6*10^{-4}$			
Au/TiONT	0	036	0.098	$8.3*10^{-4}$	$2.1*10^{-4}$			3.0

E_a Activation energy for CH_4 formation
Σ C Amount of surface carbon formed in the reaction at 493 K during 80 minutes.

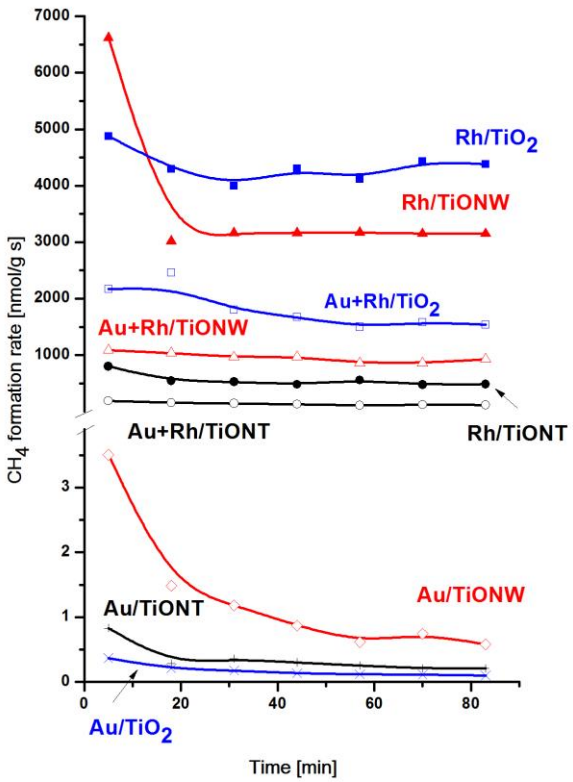

Figure. 11 Rate of methane formation on Rh/TiO_2, Rh/TiONW, Rh/TiONT, $Au–Rh/TiO_2$, Au–Rh/TiONW, Au–Rh/TiONT, Au/TiO_2, Au/TiONW, Au/TiONT catalysts at 493 K.

The activity order of the supported Rh samples in the first minutes of the reaction decreased in the order Rh/TiONW > Rh/TiO_2 > Rh/TiONT. The conversion of CO_2 on Rh/TiONW decreased significantly in time but in the other cases the CO_2 consumption was relatively stable. Rh/TiO_2 displayed the highest steady state activity. A drastic decrease in conversion was experienced when the bimetallic samples were used as catalysts but the activity order of the samples was the same. The supported Au samples were practically inactive in CO_2 hydrogenation. The less activity in the presence of Au second metal indicates that the significant part of Rh is covered by Au, but the

observed activity can be explained by distortion of the core-shell structure by reactants as it was discussed above in the case of CO interaction.

The activation energy of the reaction was determined from the temperature dependence of the CH_4 formation rate in the steady state. The values fell in the range 81–98 kJ/mol. These data are in good agreement with earlier findings [20]. There were no significant differences in the activation energies obtained on monometallic or bimetallic samples, with somewhat lower values for Au–Rh catalysts (Table 2). The amount of deposited carbon decreased in the order of TiONT> TiONW >TiO_2, with the exception of supported Au samples.

The infrared spectra registered in the DRIFT cell during the CO_2 hydrogenation showed that on Rh/TiONT (Fig. 12) and on Rh/TiONW (Fig. 13) from the beginning of the reaction an absorption band was present on the spectra in the CO region at 2045 and 2049 cm^{-1}, respectively. The intensities and the positions of these bands did not change significantly during the catalytic reaction. On Rh/NT a shoulder on the former peak was also observed at about 1960 cm^{-1}. In this case bands were detected at 1767, 1640 cm^{-1} and a weak band at 1568 cm^{-1} (Fig. 12). On Rh/NW absorptions at 1775 – 1765, 1628, 1557- 1555, and 1379 cm^{-1} were found (Fig. 13). On Rh/TiO_2 intensive absorption was detected at 2049 cm^{-1} and a weak band at 1620 and 1570 cm^{-1}. Similar spectral features were found when Au-Rh/TiONW, Au-Rh/TiONT and Au-Rh/TiO_2 was used as catalyst, only the intensities of the CO bands and the band at 1770 cm^{-1} were weaker.

The bands detected between 1550 – 1570 cm^{-1} and 1379 cm^{-1} could be assigned as asymmetric and symmetric vibration of the OCO group of formate species [91, 94-97]. The absorption found at about 1620 cm^{-1} could be attributed to water formed in the reaction. The other bands below 1700 cm^{-1} are due to different carbonates bonded to the supports [98].

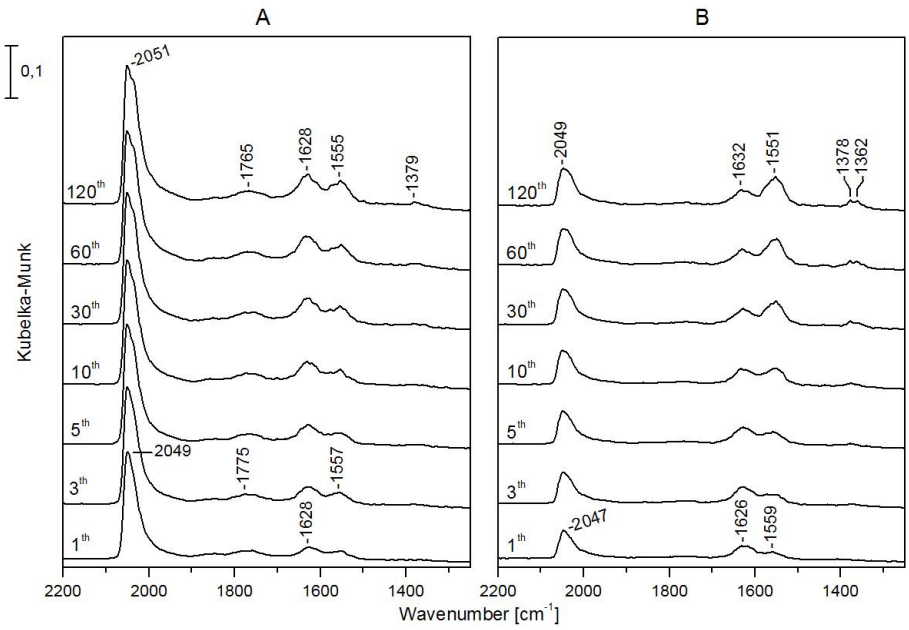

Figure 12. Infrared spectra registered during CO_2 + H_2 reaction at 493 K on Rh/NW (A) and Au-Rh/NW (B) in the different minutes of the reaction.

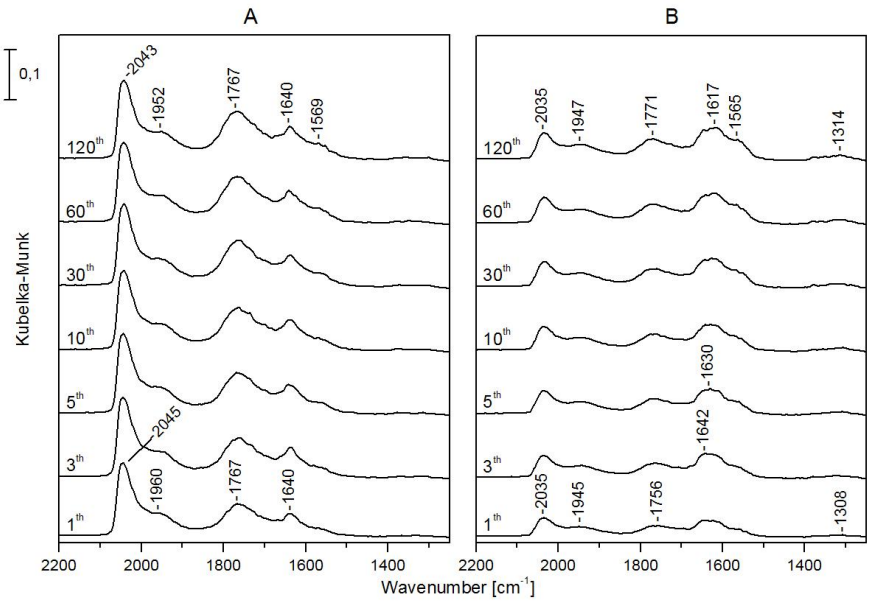

Figure 13. Infrared spectra registered during CO_2 + H_2 reaction at 493 K on Rh/NT (A) and Au-Rh/NT (B) in the different minutes of the reaction.

The assignation of the band at ~1760 cm^{-1}, detected only on titanate nanostructured support, is more complicated. This band was not obsedved on titania supported Rh catalysts [20, 88]. Tentatively we assign this band to formaldehyde of formic acid. Hoewer, the absorption band of C=O group of formaldehyde adsorbed on Rh/TiO_2 appeares at lower wave numbers at about 1727 cm^{-1} [99]. Although the vibration frequency of C=O groups in the gaseous HCOOH is at 1770 cm^{-1} [100], these feature found in our cases can not be assigned to this band because it was stable when the samples were flushed with He after the catalytic reaction. Low frequency CO vibration (under 1790 cm^{-1}) has been observed in CO adsorption on Mn, La, Ce, Fe promoted Rh/SiO_2 catalysts [101-103]. The same feature appeared on Pt/zeolites during the CO_2 hydrogenation [104]. It was suggested that Lewis acid sites caused the downward shift of CO ligand wave number with the interaction of the Lewis acid with the oxygen atom of CO. The carbon atom of chemisorbed CO bonded to Rh atom and the its oxygen tilted to the metal ion. In our cases incline to assigne the band at about 1770 cm^{-1} to such type of tilted CO which bonded to the Rh and interact with the oxygen

vacancy (Ti^{3+}) of the titanate support. When the Rh is partially covered by gold, the intensity of this band decreased or diminished (Fig. 12, Fig. 13). The tilt CO configuration is represented on Fig. 14.

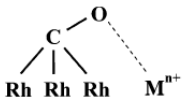

Figure 14. Sematic scheme of tilt CO configuration on Rh/titanate catalysts. M^{n+} represents Ti^{3+} site.

Taking into account the surface intermediates formed during the reaction (adsorbed CO and formate) and the reaction products (mainly methane and less extent CO) we propose that the hyrogenation of CO_2 may proceed via reversed water gas shift reaction mechanism [96, 105] and via hydrogen assisted C-O cleavage in CO or H_nCO [20, 87, 97, 106,].

$$CO_{2(a)}{}^{*} + 2H_{(a)} \rightarrow H_nCO_{(a)} + OH_{(a)} \quad (1)$$

$$H_nCO_{(a)} + H_{(a)} \rightarrow CH_x + OH_{(a)} \quad (2)$$

$$CH_{3(a)} + H_{(a)} \rightarrow CH_{4(g)} \quad (3)$$

Parallel, a realistic CO formation rout could be the decomposition of bidentate formate, too [95, 97]:

$$HCOO_{(a)} \rightarrow CO_{(a)} + OH_{(a)} \rightarrow CO_{(g)} + H_2O_{(g)} \quad (4)$$

On the other hand, formate bonded at near to metal-oxide interface decomposes forming CH_4 [94, 96]. The metallic Rh could deliver sufficient amount of hot hydrogen atoms, which raptures the C-O bond in formate species:

$$HCOO_{(a)} + 2H_{(a)} \rightarrow H_2COH_{(a)} \rightarrow H_2C_{(a)} + OH_{(a)} \quad (5)$$

$$H_2C_{(a)} + 2H_{(a)} \rightarrow CH_{4(g)} \quad (6)$$

In Na-Rh/TiONT case, formic acid formation was also detected as product [91]. It was suggested that formate species reacts with rhodium hydride:

$$HCOO_{(a)} + H_{(a)} \rightarrow HCOOH_{(g)} \quad (7)$$

[AS3] megjegyzést írt: Ez mar le lett irva? Ezt egy reviewba uj eredmenykent talan necces. De amugy ok.

[AS4] megjegyzést írt: VEgul is miert ezt mondjuk, ha az elobb beszelsz rola, hogy van csomo karbonat a felszinen es formaldehid...akkor itt nem H2CO-kat kellene irni?
Bar latom, hogy alabb irsz rola, de akkor most melyik? Itt most akkor mind a ketto lehetseges út jelolve van.

Coke formation detected after reaction can be described by the subsequent dehydrogenation of $CH_{2(a)}$.

When Na-form titantes are applied [91], the catalytic activity may be different. In the case of CO_2 hydrogenation, Yu et al. [92], compared the activity of Pt/TiONT and Pt/TiO_2 samples. In their catalytic test, the Pt/TiONT catalysts showed higher activity compared with the Pt/TiO_2. The authors related the activity of Pt/TiONT with the higher adsorption capacity of CO_2, due to its higher surface area and nanotubular morphology. Also, some active superficial species were identified by *in-situ* infrared studies during the reaction. It has been reported previously that presence of alkali metal in solid catalysts can induce the dissociation of CO_2 [11, 12, 91-93]. In the case of TiONT synthesized by hydrothermal method, the Na^+ contained in its structure could promote the effective dissociation of CO_2 on the catalyst surface, and so the rate of the CO_2 hydrogenation could be higher.

In summary, we may conclude that the structure of the support has a significant influence to the activity of titania and titante like catalyst support in CO_2 hydrogenation. Using nanowire support, the Rh/TiONW, which contains in β-TiO_2 structure during the reaction temperature, has higher activity than the Rh/TiONT, in which the anatase structure is dominant at the reaction temperature. The Degussa TiO_2, which has mainly rutile structure, exhibited somewhat higher steady state activity than Rh/TiONW although the TOF values were almost the same.

4.2 CO + H_2O reaction on Rh/TiONW, Rh/TiONT and Rh/TiO_2

Water gas, also known as synthesis gas, contains carbon monoxide (CO) and hydrogen (H_2). Water gas shift (WGS) reaction is the intermediate step used for CO reduction and hydrogen enrichment in the synthesis gas [107, 108]. In 1780, Italian physicist Felice Fontana discovered the water gas shift reaction, but its actual importance was realized much later. The water gas synthesis (WGS) reaction is an important process to produce CO-free hydrogen or to adjust the H_2/CO ratio [109]. Adjusting the H_2/CO ratio is especially required for downstream processes, such as Fischer-Tropsch reactions and methanol synthesis [110].

Many catalysts were tested in the reaction. According to the nature of the active component and the applied support, CO_2, H_2 and different hydrocarbons were formed [15, 16]. Based on

kinetic results two types of mechanisms were proposed [1]. The oxidation-reduction, or regenerative mechanism of Rideal-Elay type, in which water oxidizes the surface and CO re-reduces the oxidized surface [110]. Others describe a bi-functional process where the adsorbed CO on the precious metal or mixed metal oxide is oxidized by the support and then water fills the support oxygen vacancy [111]:

$$H_2O + * \leftrightarrow H_2 + O^* \quad (1)$$

$$CO + O^* \leftrightarrow CO_2 + * \quad (2)$$

where the $*$ is an active site.

The multi-step Langmuir–Hinshelwood type or "associative" mechanism where adsorbed or dissociated water form reactive hydroxyl groups that combine with CO to produce a formate that decomposes to CO_2 and H_2. Others describe the bifunctional nature where CO adsorbed on the reduced metal migrates to react with hydroxyl groups in bond making reaction, to produce the formate intermediate [15, 16, 107, 112-114]. FTIR analysis has been commonly used to confirm the presence of the formate intermediate:

$$CO + * \leftrightarrow CO^* \quad (3)$$

$$H_2O + 2a \leftrightarrow H^* + OH^* \quad (4)$$

$$OH^* + CO^* \leftrightarrow HCOO^* + * \quad (5)$$

$$HCOO^* + * \leftrightarrow CO_2{}^* + H^* \quad (6)$$

$$CO_2{}^* \leftrightarrow CO_2 + * \quad (7)$$

$$2H^* \leftrightarrow H_2 + 2* \quad (8)$$

At higher pressures, at industrial conditions it was necessary to include the synthesis and hydrogenation of formate [115]. In this hydrogenation reaction methanol was produced:

$$HCOO^* + H^* \leftrightarrow H_2COO^* \quad (9)$$

$$H_2COO^* + 4H^* \leftrightarrow CH_3OH_{(g)} + H_2O_{(g)} \quad (10)$$

The catalytic reaction of water with carbon monoxide to form hydrocarbons and carbon dioxide, known as the Kölbel-Engerhardt reaction [116]. Earlier this reaction was investigated over

supported rhodium [117, 118]. The formation of methane appears to occur via the water gas shift reaction, followed by the hydrogenation of surface carbon:

$$CO + 2s \leftrightarrow C_s + O_{(a)} \quad (11)$$

$$H_2O + 2s \leftrightarrow OH_{(a)} + H_{(a)} \quad (12)$$

$$C_s + 4H_{(a)} \leftrightarrow CH_{4(g)} \quad (13)$$

The turnover frequency for this reaction was a function the type of support, resulting in the turnover frequency sequence at 600 K: Rh/Al_2O_3 > Rh/Y zeolite > Rh/SiO_2 > Rh/NaY zeolite [117].

The $CO + H_2O$ reaction was investigated on Rh catalysts using titante and titania supports. The main products were hydrogen and carbon dioxide, only very small amount of methane formation was detected on titania-like supports. The catalytic activity of Rh/TiO_2, Rh/TiONW and Rh/TiONT was tested and compared at 550 K. The conversion data are displayed in Fig. 15. The CO_2 formation rates are shown in Fig. 16, H_2 formation rate shows similar trend (not shown). The highest conversion data was measured on 1% Rh/TiO_2 (Degussa P25), the steady state activity of 1% Rh/TiONW was higher than on 1% Rh/TiONT. Similar trend was found when we compared the formation rates. Although the conversion and the formation rate was the highest on 1% Rh/TiO_2 the turnover frequencies showed not significant deviation (Table 3). The effect of Au additve was also investigated.

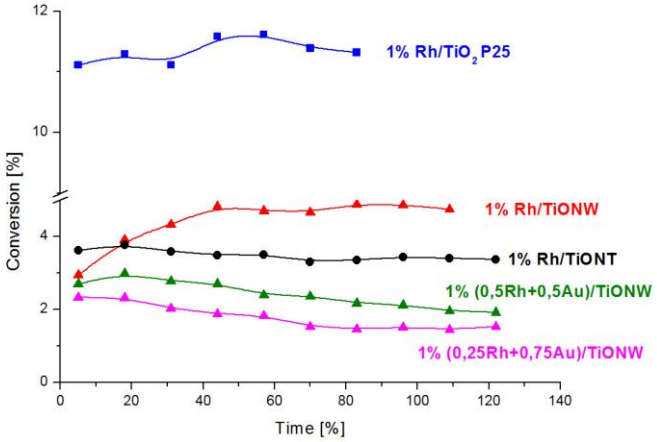

Figure 15. Conversion of CO + H_2O reaction are shown obtained on 1% Rh/TiO_2 (Degussa P25), 1% Rh/TiONW, 1% Rh/TiONT, 1% (0.25Rh + 0.75Au)/TiONW and on 1% (0.5Rh + 0.5Au)/TiONW. Reaction temperature was 550 K.

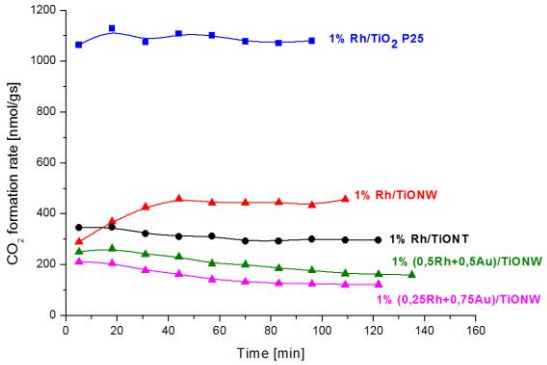

Figure 16 CO_2 formation rate in the CO + H_2O reaction on different Rh catalysts at 550 K.

Table 3. Some important activity data obtained in the CO + H_2O reaction on different catalysts.

	D %	**K %**	**WCO_2 nmol/gs**	**TOF CO_2 s^{-1}**
1% Rh/TiO_2	36	11,39	1078,07	$30,06*10^{-3}$
1% Rh/TiONT	10	3,36	295,63	$30,09*10^{-3}$
1% Rh/TiONW	29	4,74	456,79	$20,2*10^{-3}$
1% (Rh+Au)TiONW	33	1,91	176,84	$7,24*10^{-3}$

As the reaction products were almost CO_2 and hydrogen, we suggest that both oxidation-reduction, or regenerative mechanism of Rideal-Elay type, and multi-step Langmuir–Hinshelwood type or "associative" mechanism operates on titania and titanate supported Rh catalyst. The oxygen mobility, mainly in titanate supports, is high enough to subtract oxygen. On

the other hand, formate intermediates can easily formed and stabilized on these supports or metal-support interface, the CO_2 formation can be explained by the decomposition of formate.

The codeposited gold suppressed the catalytic activity as was detected in CO_2 hydrogenation indicating that the gold covers the active Rh sites. The observed smaller activity can be attributed to the gold, but we may also suggest that the reaction mixture destroys the core-shell structure as was in some cases discussed above (CO adsorption, CO oxidation).

4.3 CH_5OH decomposition

[AS5] megjegyzést írt: ERdekes hogy ezekben a reakciokban es a WGSR a degussa 25 jobb mint a titaniak.

The increasing demand for alternative energy sources drew a great attention to the ethanol transformation producing H_2 [17-19]. The use of ethanol is favored because it can be readily produced from renewable biomass. Supported noble metals were active catalyst in transformation. Both the nature of metal and support determined the product distribution. Alumina-supported catalysts are very active at low temperatures in in the dehydrogenation of ethanol to ethylene. At high temperatures, ethanol is converted into H_2, CO, CO_2 and CH_4. Rh was significantly more active and selective towards hydrogen formation than Ru, Pt and Pd [119-126]. Ethylene formation was not detected when ceria-type support was used [124]. When titania was the support, aldehyde formation was also significant [122, 123, 125]. The surface chemistry of ethanol on Rh single crystal was also investigated in detail [127, 128]. In this study, we compare the supported Rh on different nanostructured titanates (TiONW and TiONT) catalysts in ethanol transformation reaction.

The 1% Rh/TiO_2 showed a high conversion at 603 K at the first stage of the reaction, at 5 min the conversion reached the 93%. With increasing reaction time, the conversion significantly dropped (Fig. 17). The steady state activity was obtained with ~ 40% conversion at around 120 min.

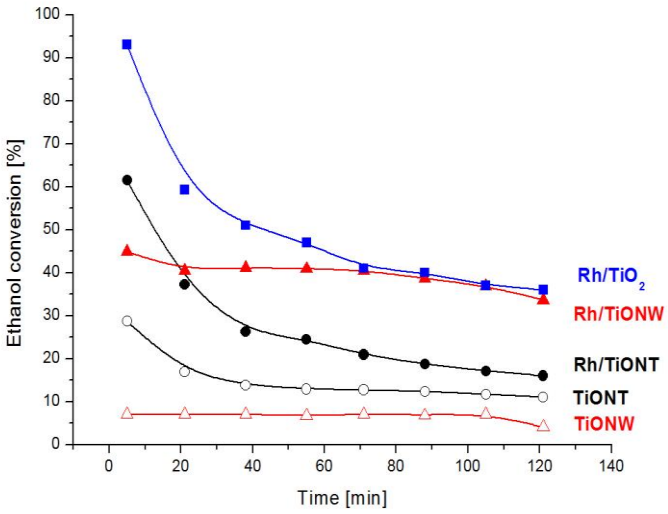

Figure 17. Ethanol conversion obtained on titania and titanate supported Rh catalysts at 60K.

When nanostructured titanates were applied, the activities were less. In the case of 1% Rh/TiONT, the initial conversion was around 60 %, it decreased with time, the steady state activity was obtained at around 100 min with 20 % conversion. Interestingly the Rh/TiONW activity was higher than that of Rh/TiONT without activity decrease (Fig. 17). The steady state activity was the same as was measured on Rh/TiO_2. All titania and titanate supported Rh catalysts acetaldehyde, hydrogen, carbon monoxide, methane, ethylene and diethyl ether were the reaction products. Sometimes very small amounts of aceton and acetic acid were detectable. High acetaldehyde selectivity was detected in all cases which indicates that the acetaldehyde forms via oxidative dehydrogenation of ethanol as was supposed earlier on reducible oxide support, including TiO_2 [123]. The relatively lower catalytic activity in the case of Rh/TiONT can be explained by the tube structure; the diameter of the tube prevent the ethanol to reach the active site insight of the tube.

[AS6] megjegyzést írt: And also it is possible that the special rutile/anatase equilubrium int he degussa p25 is favoring the reactons. This can be boosted int he case of the tubes and wires also after the proper heat treatment as observed in chapter Experimentals…

The selectivity data at 5 and 105 min of the reaction are presented in Table 4. On Rh/TiO_2 the acetaldehyde selectivity increased with time and the hydrogen selectivity decreased. This decreasing was much less on both Rh/TiONW and Rh/TiONT, the hydrogen selectivity at steady

state activity was ~10%. This hydrogen selectivity value is significantly higher than on Rh/TiO_2. The ethylene and diethyl ether selectivity were rather low in all cases.

Table 4. Conversion and selectivity data measured in ethanol transformation reaction on titania and titante supported Rh catalysts.

	Conversion %		**Selectivity %**							
			C_2H_4		**C_2H_4O**		**H_2**		**$(C_2H_5)O$**	
min	**5.**	**105.**	**5.**	**105.**	**5.**	**105.**	**5.**	**105.**	**5.**	**105.**
Rh/TiO_2	93	37	6.9	1.8	77.8	95.7	13.6	5.8	7	0.1
Rh/TiONW	44	36	0.4	0.2	86.6	94.7	12.5	10.8	3.7	0.6
Rh/TiONT	61	17	0.4	0.3	78.0	91.3	25.0	10.6	1.0	3.6
TiONW	1	7.1	3.2	3.4	66.7	66.1	5.0	0	26.0	28.0
TiONT	28.7	11.7	23	0.8	93	96.0	6.0	0	1.0	2.4

The infrared spectroscopy is a useful tool to determine the surface intermediates formed during the catalytic reaction. In situ DRIFTS study were performed in the presence of reaction mixture at different temperatures. The spectra were qualitatively the same on all supported catalysts. For demonstration, Fig.18 shows the typical spectra obtained on Rh/TiONW.

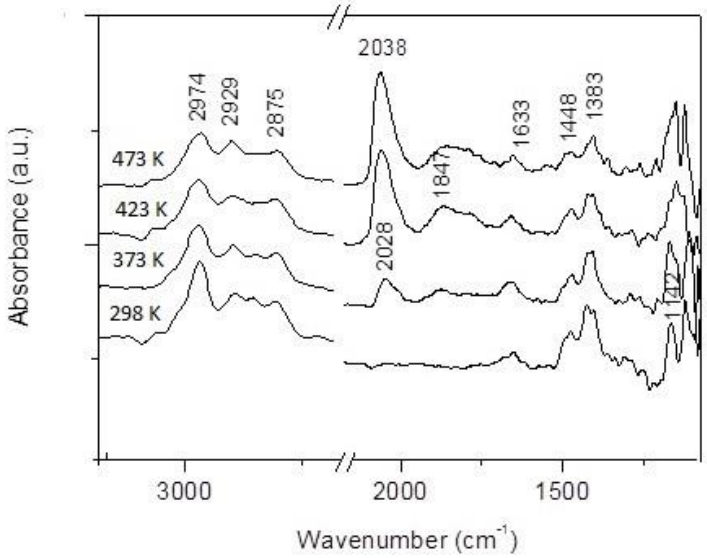

Figure 18. DRIFT spectra obtained on Rh/TiONW during the ethanol decomposition at different temperature. Partially reproduced from Ref. [57].

At 300 K absorption bands were observed at 2974, 2929 and 2875 cm−1 in the C–H stretching region. In the low frequency range absorption bands were detected at 1448–1450 and 1383–1384 cm−1, both could be assigned as symmetric and asymmetric CH_3 vibrations of ethanol/ethoxide. The bands observed at 1140–1144, 1124–1121, 1069–1074, 1045–1047 cm^{-1} could be attributed to νC–O and C–C vibrations of monodentate and bidentate ethoxide species [122-125]. The intensities of these bands decreased as the temperature increased but dramatic changes were not detected. At ~1560 cm^{-1} a small intensity peak appeared from 423 K, probably due to acetate species (ν_{as}O-C-O). This band appears with higher intensity on Al_2O_3 or CeO_2 support [122-124].

Apart from the ethanol/ethoxide bands, a peak at 1633 cm^{-1} started developing at 297 K. Its intensity increased slightly with temperature. This band is present in many cases in ethanol decomposition, oxidation and ethanol steam reforming [129, 130]. It was attributed to νC–O

vibration in acetyl (CH_3CO) species. When the Rh/TiO_2 was treated with ethanol above 373 K new peaks were detected at 2028 and 1847 cm^{-1}. The intensities of these bands increased with increasing the temperature and the peak observed at 2028 cm^{-1} at room temperature shifted to higher wave numbers. The absorbance at 1847 cm^{-1} could be attributed to bridge bonded CO on Rh sites [71, 122]. The feature of the adsorbed CO detected at 2028–2038 cm^{-1} is significantly differing from that depicted in Fig. 5. This discrepancy could be explained by the Rh carbonyl hydride formation (H–Rh–CO) [122, 131]. The adsorbed CO desorbs in a desorption rate limiting step.

Taking into account the reaction products and the surface intermediates formed during the reaction we offer the following reaction steps which were proved in many cases [17, 19, 119, 123-125]. After the initial step, the formation of ethoxide, further dehydrogenation occurs:

$$C_2H_5OH_{(a)} \rightarrow C_2H_5O_{(a)} + H_{(a)} \quad (1)$$

$$C_2H_5O_{(a)} \rightarrow CH_3CHO_{(a)} + H_{(a)} \quad (2)$$

The acetaldehyde mostly desorbs as reaction product, and a smaller fraction decomposes forming acetyl:

$$CH_3CHO_{(a)} \rightarrow CH_3CO_{(a)} + H_{(a)} \quad (3)$$

In the acetyl species the C-C rupture easily happens forming adsorbed CO and methyl radicals. Rh is considered to be among the best metals for hydrogen production due to its high activity for C-C break in ethanol. The methyl radicals either decomposes further or reacts with hydrogen and finally methane is produced. The adsorbed hydrogen recombines giving H_2 formation. During ethanol decomposition, very small amounts of ethylene and diethyl ether formation were detected. In this process the first step involves the formation of diethyl ether as a results of intermolecular dehydrogenation of two ethanol molecules [132]:

$$2C_2H_5OH_{(a)} \rightarrow C_2H_5\text{-}O\text{-}C_2H_{5(a)} + 2OH_{(a)} \quad (4)$$

This is followed by a second dehydrogenation of diethyl ether to ethylene:

$$C_2H_5\text{-}O\text{-}C_2H_{5(a)} \rightarrow 2C_2H_{4(a)} + 2H_{(a)} \quad (5)$$

Summing up, we may conclude that the structure of nanotitanate influences the steady state conversion of ethanol was equal on Rh/TiO_2 and TiONW. Due to the tubular structure of TiONT

the decomposition is sterically hindered. There was no significant difference in selectivity; in all cases, acetaldehyde was the main product. It remarkable that on Rh supported on nanostructured titanates the hydrogen selectivity was double at steady state conditions. IR studies showed that the ethoxide dehydrogenates, most of acetaldehyde desorbs as product, a smaller part dehydrogenates further and the C-C bond rupture occurs in the acetyl surface intermediate.

5. Summary remarks

Rhodium induced phase transformation of titanate nanostructures was studied by Ramman, x-ray diffraction and high-resolution transmission electron spectroscopy. Rh accelerated the transformation of titanate nanotubes to anatase phase. Rh decorated nanowire transform into the β-TiO_2 structure, where their pristine counterparts' recrystallize into anatase. Rh assisted processes started from 550 K where the titante supported Rh catalysts exhibited remarkable catalytic effect in CO_2 hydrogenation, CO + H_2O reaction and in ethanol decomposition.

The activity order of the supported Rh samples in the first minutes of the reaction decreased in the order Rh/TiONW > Rh/TiO_2 > Rh/TiONT. The conversion of CO_2 on Rh/TiONW decreased significantly in time but in the other cases the CO_2 consumption was relatively stable. Rh/TiO_2 displayed the highest steady state activity. The reaction run in all cases via formation of formate intermediate, on both nanostructured titantes a "tilted CO" species are also formed in which a H-assisted C-O bond may easily rupture.

In the CO + H_2O reaction the highest conversion was obtained on Rh/TiO_2 Degussa P25 catalyst. It is very interesting that the turnover frequencies obtained in the case of Rh/TiONT, Rh/TiONW and Rh/TiO_2 were almost the same. From this comparison we may suggest that the number of available Rh atoms at the surface is significantly higher in nanotitanates. As the reaction products were almost CO_2 and hydrogen, we suggest that both oxidation-reduction, or regenerative mechanism of Rideal-Elay type, and multi-step Langmuir–Hinshelwood type or "associative" mechanism operates. The oxygen mobility, mainly in titanate supports, is high enough to subtract oxygen for the reaction.

In ethanol decomposition, the Rh/TiO_2 and Rh/TiONW showed equal steady state activity. The relatively lower catalytic activity in the case of Rh/TiONT can be explained by the tube structure;

the diameter of the tube prevent the ethanol to reach the active site insight of the tube. In all cases, acetaldehyde was the main product. It remarkable that on nanostructured titanates the hydrogen selectivity higher than on Rh/TiO_2 at steady state conditions.

Acknowledgements

The authors wish to thank Dr. Péter Pusztai and Mrs Kornelia Baán for executing the electomicroscopic and infrared measurements and also Prof. András Erdőhelyi for fruitful discussions. Financial support of this work by the National Research Development and Innovation Office through grants GINOP-2.3.2-15-2016-00013 and NKFIH OTKA K120115 (Z.K.) and K126065 (A.K.) and OTKa PD 120877 (A. S.) is gratefully acknowledged.

References

1. Ertl, G.; Knözinger, H.; Weitkamp, J., Handbook of Heterogeneous Catalysis, VCH; Weinheim, **1997,** p 5 v (xxiiv, 2478 pp)
2. Wang, W.; Wang, S.; Ma, X.; Gong, J., Recent advances in catalytic hydrogenation of carbon dioxide. *Chem. Soc. Rev.* 2011, 40, 3703-3727.
3. Centi, G.; Quadrelli, E.A.; Perathoner, S. Catalysis for CO_2 conversion: a key technology for rapid introduction of renewable energy in the value chain of chemical industries. *Energy & Environ. Sci.* 2013, 6, 1711-1731.
4. Artz, J.; Müller, T.E.; Thenert, K.; Kleinekorte, J.; Meys, R.; Sternberg, A.; Bardow, A.; Leitner, W., Sustainable conversion of carbon dioxide: an integrated review of catalysis and life cycle assessment. *Chem. Rev.* **2017**, 118, 434-504.
5. Kondratenko, E.V.; Mul, G.; Baltrusaitis, J.; Larrazábal, G.O.; Pérez-Ramírez, J., Status and perspectives of CO_2 conversion into fuels and chemicals by catalytic, photocatalytic and electrocatalytic processes. *Energy & Environ. Sci.* **2013**, *6* (11), 3112-3135.

6. Studt, F.; Sharafutdinov, I.; Abild-Pedersen, F.; Elkjær, C.F.; Hummelshøj, J.S.; Dahl, S.; Chorkendorff, I.; Nørskov, J.K., Discovery of a Ni-Ga catalyst for carbon dioxide reduction to methanol. *Nat. Chem.* **2014,** *6*, 320-324.

7. Porosoff, M.D.; Yan, B.; Chen, J.G., Catalytic reduction of CO_2 by H_2 for synthesis of CO, methanol and hydrocarbons: challenges and opportunities. *Energy & Environ. Sci.* **2016**, *9*, 62-73.

8. Leonzio, G., State of art and perspectives about the production of methanol, dimethyl ether and syngas by carbon dioxide hydrogenation. *J. of CO_2 Util.* 2018, *27*, 326-354.

9. Zheng, Y.; Zhang, W.; Li, Y.; Chen, J.; Yu, B.; Wang, J.; Zhang, L.; Zhang, J., Energy related CO_2 conversion and utilization: advanced materials/nanomaterials, reaction mechanisms and technologies. *Nano Energy* 2017, 40, 512-539.

10. Frontera, P.; Macario, A.; Ferraro, M.; Antonucci, P., Supported catalysts for CO_2 methanation: a review. *Catalysts* 2017, *7*, 59.

11. Freund, H.J., Roberts, M.W., Surface chemistry of carbon dioxide. *Surf. Sci. Rep.* 1996, 25, 225-273.

12. Kiss J, Révész, K, Solymosi, F. Photoelectron Spectroscopic Studies of the Adsorption of CO_2 on Potassium-Promoted Rh(111). *Surf. Sci.* **1988**, 207, 36-54.

13. László, B.; Baán, K.; Varga, E.; Oszkó, A.; Erdőhelyi, A., Kónya, Z.; Kiss, J., Photo-induced reactions in the CO_2-methane system on titanate nanotubes modified with Au and Rh nanoparticles. *Appl. Catal. B: Environ.* **2016,** 199, 473-484.

14. Kiss, J.; Kukovecz, Á.; Kónya, Z., Beyond Nanoparticles; The Role of Sub-nanosized Metal Species in Heterogeneous Catalysis. *Catal. Lett*. 2019, 149, 1441-1454.

15. Pal, D.B.; Chand, R., Upadhyay, S.N; Mishra, P.K., Performance of water gas shift reaction catalysts: A Review. *Renewable and Sustainable Energy Reviews* **2018,** 93, 549-565.

16. Ratnasamy, C.; Wagner, J.P., Water Gas Shift Catalysis. *Catal.Rev.***2009,** 51, 325-440.

17. Mattos, L.V.; Jacobs, G.; Davis, B.H.; Noronha, F.B., Production of hydrogen from ethanol: Review of reaction mechanism and catalytic deactivation. *Chem. Rev.* **2012,** 112, 4094-4123.

18. Contreras, J.L.; Salmones, J.; Colin-Luna, J.A.; Nuno, L.; Quintana, B.; Cordova, I.; Zeifert, B.H.; Tapia, C.; Fuentes; G.A., Catayst for H_2 production using the ethanol steam reforming (a review). *Int. J. of Hydrogen Energy*, **2014,** 39, 18835-18853.

19. Punase, K.D.; Rao, N.; Vija, P., A review on mechanistic kinetic models of ethanol steam reforming for hydrogen production using a fixed bed reactor. *Chem. Papers* **2019,** 73, 1027-1042.

20. Solymosi F.; Erdőhelyi, A.; Bánsági, T., Methanation of CO_2 on supported rhodium catalyst. *J. Catal*. **1981,** 68, 371-382.

21. Henderson, M.A.; Worley, S.D. An infrared study of the hydrogenation of carbon dioxide on supported rhodium catalysts. *J. Phys. Chem.* **1985**, 89, 1417-1423.

22. Trovarelli, A.; Mustazza, C.; Dolcetti, G.; Kaspar, F.; Grazioni, M., Carbon-dioxide hydrogenation on Rhodium supported on transition-metal oxides - effect of reduction temperature on product distribution. *Appl. Catal*. **1990**, 65, 129-142.

23. Solymosi, F.;, Tombácz, I.; Koszta, J., Effect of variation of electric properties of TiO_2 support on hydrogenation of CO and CO_2 over Rh catalysts. *J. Catal*. **1985,** 95, 578-586.

24. Zhang, Z. L.; Kladi, A.; Verykios, X. E., Effects of Carrier Doping on Kinetic Parameters of CO_2 Hydrogenation on Supported Rhodium. *Catalysts. J. Catal*. **1994**, 148, 737-747.

25. Diebold, U., The surface science of titanium dioxide. *Surf. Sci. Rep.* **2003**, 48, 53-229.

26. Henderson, M.A., A surface science perspective on photocatalysis. *Surf. Sci. Rep.* **2011**, 66, 185-297.
27. Wang, L.; Sasaki, T., Titanium Oxide Nanosheets: Graphene Analogues with Versatile Functionalities. *Chem. Rev*. **2014**, 114, 9455-9486.
28. Peña, M.A.; Fierro, J.L.G., Chemical Structures and Performance of Perovskite Oxides. *Chem. Rev*. **2001**, 101, 1981-2018.
29. Roy, P.; Berger, S.; Schmuki, P. TiO_2 nanotubes: synthesis and applications. *Angew. Chem. Int. Ed. Engl*. **2011**, 50 (13), 2904-2939.
30. Macák, J.M.; Tsuchiya, H.; Schmiuki, P. High-aspect-ratio TiO_2 nanotubes by anodization of titanium. *Angew. Chem. Int. Ed. Engl*. **2005**, 44, 2100-2102.
31. Bavykin D. V., Lapkin A.A.; Plucinski, P.K.; Friderich, J.M.; Walsh, F.C., Reversible Storage of Molecular Hydrogen by Sorption into Multilayered TiO_2 Nanotubes. *J. Phys. Chem. B*, **2005**, 109, 19422-19427.
32. Huang, R.W.J.M.; Chung, F.; Kelder, E.M. Impedance Simulation of a Li-Ion Battery with Porous Electrodes and Spherical Li^+. *Intercalation Particles. J. Electrochem. Soc.*, **2006**, 153, A1459-A1465.
33. Kukovecz, Á.; Pótári, G.; Oszkó, A.; Kónya, Z.; Erdőhelyi, A.; Kiss, J., Probing the interaction of Au, Rh and bimetallic Au-Rh clusters with the TiO_2 nanowire and nanotube support. *Surf. Sci*. **2011**, 605, 1048-1055.
34. Madarász, D.; Pótári, G.; Sápi, A.; László, B.; Csudai, C., Oszkó, A.; Kukovecz, Á.; Erdőhelyi, A.; Kónya, Z.; Kiss, J., Metal loading determines the stabilization pathway for Co^{2+} in the titanate nanowires: ion exchange vs. cluster formation. *J. Phys. Chem. Chem. Phys.* **2013**, 15, 15917-15925.

35. Kasuga, T.; Hiramatsu, M.; Hoson, A.; Sekino, T.; Niihara, K., Formation of Titanium Oxide Nanotube. *Langmuir*, **1998**, 14, 3160-3163.

36. Horváth, E.; Kukovecz, Á.; Kónya, Z.; Kiricsi, I., Hydrothermal Conversion of Self-Assembled Titanate Nanotubes into Nanowires in a Revolving Autoclave, *Chem. Mater*. **2007**,19, 927-931.

37. Kukovecz, Á.; Hodos, M.; Horváth, E.; Radnóczi, G.; Kónya, Z.; Kiricsi, I., Oriented Crystal Growth Model Explains the Formation of Titania Nanotubes. *J. Phys. Chem. B* **2005**,109, 17781-17783.

38. Torrente-Murciano, L.; Lapkin, A.A.; Chadwick D**.,** Synthesis of high aspect ratio titanate nanotubes. *J. Mater. Chem*, 2010, 20, 6484-6489.

39. Sun, X.; Li, Y**.,** Synthesis and Characterization of Ion-Exchangeable Titanate Nanotubes. *Chem. Eur. J*. 2003, 9, 2229-2238.

40. Cesano, F.; Bertarione, S.; Uddin, M.J.; Agostini, G.; Scarano, D.; Zeccina, A., Designing TiO_2 Based Nanostructures by Control of Surface Morphology of Pure and Silver Loaded Titanate Nanotubes. *J. Phys. Chem. C* **2010**, 114, 169-178.

41. Pusztai, P.; Puskás, R.; Varga, E.; Erdőhelyi, A.; Kukovecz, Á.; Kónya, Z.; Kiss, J., Influence of gold additives ont he stability and phase transformation of titanate nanostructures. *Phys. Chem. Chem. Phys.* **2014**, 16, 26786-26797.

42. Bavykin, D.V.; Walsh, F.C., Titanate and Titania Nanotubes: Synthesis, Properties and Application, RSC Publishing, Cambridge, **2010**.

43. Kukovecz, Á.; Kordás, K.; Kiss, J.; Kónya, Z., Atomic scale characterization and surface chemistry of metal modified titanate nanotubes and nanowires. *Surf. Sci. Rep.* **2016,** 71, 473-546.

44. Bavykin, D.V.; Friedrich, J.M.; Walsh, F.C**.,** Protonated Titanates and TiO_2 Nanostructured Materials: Synthesis, Properties, and Applications. *Advanced Mater.* 2006, 18, 2807–2824.

45. Kiss, J.; Pusztai, P.; Óvári, L.; Baán, K.; Merza, G.; Erdőhelyi, A.; Kukovecz, Á.; Kónya, Z., Decoration of Titanate Nanowires and Nanotubes by Gold Nanoparticles: XPS, HRTEM and XRD Characterizatione. *J. Surf. Sci. and Nanotechnol.* **2014,** 12, 252-258.

46. Akita, T.; Okumura, M.; Tanaka, K.; Ohkuma, K.; Kohyama, M.; Koyanagi, T.; Data, M.; Tsubota, S.; Haruta, M.**,** Transmission electron microscopy observation of the structure of TiO_2 nanotube and Au/TiO_2 nanotube catalyst. *Surf. and Interf. Anal.* 2005, 37, 265-269.

47. Malwadkar, S.S.; Gholap, R.S.; Awate, S.V.; Korake, P.V.; Chaskar, M.G.; Gupta, N.M.**,** Physico-chemical, photo-catalytic and O_2-adsorption properties of TiO_2 nanotubes coated with gold nanoparticles. *Photochem. Photobiol. A: Chem.* 2009, 203, 24-31.

48. Turki, A.; Kochkar, H.; Guillard, C.; Berhault, G.; Ghorbel, A.**,** Effect of Na content and thermal treatment of titanate nanotubes on the photocatalytic degradation of formic acid. *Appl. Catal. B: Envir.* 2013,138-139, 401-415.

49. Idakiev, V.; Yuan, Z.Y.; Tabakova, T.; Su, B.L. Titanium oxide nanotubes as supports of nano-sized gold catalysts for low temperature water-gas shift reaction. *Appl. Catal. A General*, 2005, 281, 149-155.

50. Méndez-Cruz, M.; Ramírez-Solís ,J.; Zanella, R. CO oxidation on gold nanoparticles supported over titanium oxide nanotubes. *Catal. Today* 2011, 166, 172-179.

51. Zhu, B.; Guo, Q.; Huang, X.; Wang, S.; Zhang, S.; Wu, S.; Huang, W.**,** Characterization and catalytic performance of TiO_2 nanotubes-supported gold and copper particles. *J. Mol. Catal. A: Chem.* 2006, 249, 211-217.

52. László, B.; Baán, K.; Ferencz, Z., Galbács, G.; Oszkó, A.; Kiss, J.; Kónya, Z.; Erdőhelyi, A., Gold size effect in the thermal-induced reaction of CO_2 and H_2 on titania and titanate nanotube-supported gold catalysts. *J. of Nanosci. and Nanotechnol.* **2019**, 19, 470-477.

53. László, B.; Baán, K.; Oszkó, A.; Erdőhelyi, A.; Kiss, J.; Kónya, Z., Hydrogen evolution in the photocatalytic reaction between methane and water in the presence of CO_2 on titanate and titania supported Rh an Au catalysts. *Top.in Catal.* **2018,** 61, 875-888.

54. Kiss, J.; Németh, R.; Koós, Á.; Raskó, J., Characterization of Au-Rh/TiO_2 Bimetallic Nanocatalysts by CO and CH_3CN Adsorption: XPS, TEM and FTIR Measurements. *J. Nanosci. Nanotech.* **2009,** 9, 3828-3836.

55. Oszkó, A.; Pótári, G.; Erdőhelyi, A.; Kukovecz, Á.; Kónya, Z.; Kiricsi, I.; Kiss, J., Structure of Au-Rh bimetallic system formed on titanate nanowires and nanotubes. *Vacuum* **2011,** 85, 1114-1119.

56. Kiss, J.; Óvári, L.; Oszkó, A.; Pótári, G.; Tóth, M.; Baán, K.; Erdőhelyi, A. Structure and reactivity of Au-Rh bimetallic clusters on titanate nanowires, nanotubes and TiO_2(110). *Catal. Today* **2012,** 181, 163-170.

57. Tóth, M.; Kiss, J.; Oszkó, A.; Pótári, G.; László, B.; Erdőhelyi, A., Hydrogenation of Carbon Dioxide on Rh, Au and Au-Rh Bimetallic Clusters Supported on Titanate Nanotubes, Nanowires and TiO_2. *Top. in Catal.* **2012,** 55, 747-756.

58. Pótári, G.; Madarász, D.; Nagy, L.; László, B.; Sápi, A.; Oszkó, A.; Kukovecz, A.; Erdőhelyi, A.; Kónya, Z.; Kiss, J., Rh-induced Support Transformation Phenomena in Titanate Nanowire and Nanotube Catalysts. *Langmuir* **2013,** 29, 3061-3072.

59. Kolen'ko, Y.V.; Kovnir, K.A.; Gavrilov, A.I.; Garshev, A.V.; Frantti, J.; Lebedev, O.I.; Churagulov, B.R.; Van Tendeloo, G.; Yoshimura, M., Hydrothermal Synthesis and Characterization of Nanorods of Various Titanates and Titanium Dioxide. *J. Phys. Chem. B.* **2006**, 110, 4030-4038.

60. Ma, R.; Fukuda, K.; Sasaki, T.; Osada, M.; Bando, Y., Structural Features of Titanate Nanotubes/Nanobelts Revealed by Raman, X-ray Absorption Fine Structure and Electron Diffraction Characterizations. *J. Phys. Chem. B* **2005**, 109, 6210-6214.

61. Ohsaka, T.; Izumi, F.; Fujiki, Y., Raman spectrum of anatase, TiO_2. *J. Raman Spec.* **1978**, 7, 321-324.

62. Du, Y.L.; Deng, Y.; Zhang, M.S., Variable-temperature Raman scattering study on anatase titanium dioxide nanocrystals. *J. Phys. Chem. Solids* **2006**, 67, 2405-2408.

63. Scepanovic, M.J.; Grujic-Brojcin, M.; Dohcevic-Mitrovic, Z.D.; Popovic, Z.V., Characterization of Anatase TiO_2 Nanopowder by Variable-Temperature Raman Spectroscopy. *Science of Sintering* **2009**, 41, 67-73.

64. Wang, G.; Liu, Z.Y.; Wu, J.N.; Lu, Q. Preparation and electrochemical capacitance behavior of TiO_2-B nanotubes for hybrid supercapacitor. *Materials Letters*, **2012**, 71, 120-122.

65. Poirier, G.E.; Hance, B.K.; White, J.M., Scanning tunneling microscopic and Auger electron spectroscopic characterization of a model catalyst: rhodium on titania(001). J. *Phys. Chem.* **1993**, 97, 5965-5972.

66. Berkó, A.; Ménesi, G.; Solymosi, F., STM study of rhodium deposition on the TiO_2(110)-(1x2) surface. *Surf. Sci.* **1997,** 372, 202-210.

67. Óvári, L.; Kiss, J. Growth of Rh nanoclusters on TiO_2(110): XPS and LEIS studies. *Appl. Surf. Sci*. **2006**, 252, 8624-8629.

68. Evans, J.; Hayden, B.E.; Newton, M.A., A comparison of the chemistry of $Rh^{I}(acac)(CO)_2$ and $Rh^{I}(CO)_2Cl$ adsorbed on TiO2[110]: development of particulate Rh and oxidative disruption by CO. *Surf. Sci*. **2000**, 462, 169-180.

69. Khosravian, H.; Liang, Z.; Uhl, A.; Trenary, M.; Meyer, R., Controlled Synthesis of Rh Nanoparticles on TiO_2(110) via $Rh(CO)_2$(acac). *J. Phys. Chem. C* **2012**, 116, 11987-11993.

70. Berkó, A.; Ménesi, G.; Solymosi, F., Scanning tunneling microscopy study of the CO-induced structural changes of Rh crystallites supported by TiO_2(110). *J. Phys. Chem*. **1996**, 100, 17732-17734.

71. Solymosi, F.; Pásztor, M., An infrared study of CO chemisorption on the topology of supported rhodium. *J. Phys. Chem*. **1985,** 89, 4789-4793.

72. Prime M.**,** Infrared study of CO chemisorption on zeolite and alumina supported rhodium. *J. Chem. Soc. Faraday Trans.1*. 1978, 74, 2570-2580.

73. Rice, C.A.; Worley, S.D.; Curtis, C.W.; Guin, J.A.; Tarrer, A.R., The oxidation state of dispersed Rh on Al_2O_3. *J. Chem. Phys*. **1981**, 74, 6487-6497.

74. Varga, E.; Pusztai, P.; Oszkó, A.; Baán, K.; Erdőhelyi, A.; Kónya, Z.; Kiss, J., Stability and Temperature-induced Agglomerization of Rh Nanoparticles Supported by CeO_2, *Langmuir*, **2016**, 32, 2761-2770.

75. Kibis, L.S.; Svintsitskiy, D.A.; Derevyannikova, E.A.; Kardash, T.Y.; Slavinskaya, E.M.; Svetlichnyi, V.A.; Boronin, A.I., From high dispersed Rh^{3+} to nanoclusters and nanoparticles: Probing the low-temperature NO+CO activity of Rh-doped CeO_2 catalysts. *Appl. Surf. Sci*. **2019,** 493, 1055-1066.

76. Idriss, H.; Llorca, J., Low Temperature Infrared Study of Carbon Monoxide Adsorption on Rh/CeO_2. *Catalysts* **2019,** 9, 598-601.

77. Henry, C.R. Surface studies of supported model catalysts. *Surf. Sci. Rep*. **1988**, 31, 231-233.

78. Solymosi, F. Importance of the electric properties of supports in the carrier effect. *Catal. Rev.* **1967**, 1, 233-255.

79. Sasahara, A.; Pang, C.L.; Onishi, H., Probe Microscope Observation of Platinum Atoms Deposited on the TiO_2(110)-(1 × 1) Surface. *J. Phys. Chem. B* **2006**, 110, 13453-13457.
80. Sasahara, A.; Pang, C.L.; Onishi, H. Local Work Function of Pt Clusters Vacuum-Deposited on a TiO_2 Surface. *J. Phys. Chem. B* **2006**, 110, 17584-17588.
81. Óvári, L.; Bugyi, L.; Majzik, Zs.; Berko, A.; Kiss, J., Surface Structure and Composition of Au-Rh Bimetallic nanoclusters on TiO_2(110): a LEIS and STM study. *J. Phys. Chem. C* 2008,112, 18011-18016.
82. Óvár,i L.; Berkó, A.; Balázs, N.; Majzik, Zs.; Kiss, J., Formation of Rh−Au Core−Shell Nanoparticles on TiO_2(110) Surface Studied by STM and LEIS. *Langmuir* **2010**, 26, 2167-2175.
83. Palotás, K.; Óvári, L.; Vári, G.; Gubó, R.; Farkas, A.P.; Kiss, J.; Berkó, A.; Kónya, Z., Au-Rh surface structures on Rh(111): DFT-insights to the formation of an ordered surface alloy. *Journal of Physical Chemistry C* **2018,** 122, 22435–22447.
84. Tenny, S.A.; Ratliff, J.S.; Roberts, C.C.; He, W.; Ammal, S.C.; Heyden, A.; Chen, D.A. Adsorbate-Induced Changes in the Surface Composition of Bimetallic Clusters: Pt−Au on TiO_2(110). *Chen, J. Phys. Chem.* C **2010**, 114, 21652-21663.
85. Gao, F.; Wang, Y.; Goodman, D.W., Reaction Kinetics and Polarization-Modulation Infrared Reflection Absorption Spectroscopy (PM-IRAS) Investigation of CO Oxidation over Supported Pd−Au Alloy Catalysts, *J. Phys. Chem. C* **2010**, 114, 4036-4043.
86. Ozturk, O.; Park., J.B.; Ma, S.; Ratliff, J.S.; Zhou, J.; Mullins ,D.R., Chen, D.A., Probing the interactions of Pt, Rh and bimetallic Pt–Rh clusters with the TiO_2(110) support. *Surf. Sci.* **2007**, 601, 3099-3113.
87. Ferrando, R.; Jellinek, J.; Johnson, R.I., Nanoalloys: From Theory to Applications of Alloy Clusters and Nanoparticles. *Chem. Rev.* **2008**, 108, 845-910.
88. Solymosi, F.; Bánsági, T.; Erdőhelyi, A., Infrared study of the surface interaction between H_2 and CO_2 over rhodium on various supports *J. Chem. Soc. Faraday Trans.* **1981,** 77, 2645-2657.

89. Inoune, T.; Iizuka, T.; Tanabe, K., Hydrogenation of carbon dioxide and carbon monoxide over supported rhodium catalysts under 10 bar pressure. *Appl. Catal.* **1989**, 46, 1-9.

90. Novák, E.; Fodor, K.; Szailer, T.; Oszkó, A.; Erdőhelyi, A., CO_2 Hydrogenation on Rh/TiO_2 Previously Reduced at Different Temperatures. *Top. Catal.* **2002**, 20, 107-117.

91. Ruiz-Gracia, J.R.; Fierro-Gonzales, J.C.; Handy, B.E.; Hinojosa-Reyes, L.; De Haro Del Rio, D.A.; Lucio-Ortiz, C.J.; Valle-Cervantes, S.; Flores-Escamilla, G.A., An In Situ Infrared Study of CO_2 Hydrogenation to formic Acid by Using Rhodium Supported on Titanate Nanotubes as Catalysts. *ChemistrySelect* **2019,** 4, 4206-4216.

92. Yu, K.P.; Yu, W.Y.; Kuo, M.C.; Liou, Y.C.; Chien, S.H. Pt/titante-nanotubes; A potential catalyst for CO_2 hydrogenation. *Appl. Catal. B* **2008,** 281, 112-118.

93. Farkas, A.P.; Solymosi, F., Activation and reaction of CO_2 on K-promoted Au(111) surface. *J. Phys. Chem. C* **2009,** 113, 19930-19936.

94. Wang, X.; Shi, H.; Kwak, J.H.; Szanyi, J., Mechanism of CO_2 hydrogenation on Pt/Al_2O_3 Catalysts. *J. ACS Catal*. **2015**, *5* (11), 6337–6349.

95. Kecskés, T.; Raskó, J.; Kiss, J. FTIR and mass spectrometric studies on the interaction of formaldehyde with TiO_2 supported Pt and Au catalysts. *Appl. Catal. A Gen.* **2004**, 273, 55–62.

96. Sápi, A.; Halasi, G.; Kiss, J.; Dobó, D.G.; Juhász, K.L.; Kolcsár, V.J.; Ferencz, Z.; Vári, G.; Matolin, V.; Erdőhelyi, A.; Kukovecz, Á.; Kónya, Z., In Situ DRIFTS and NAP-XPS Exploration of the Complexity of CO_2 Hydrogenation over Size-Controlled Pt Nanoparticles Supported on Mesoporous NiO. *J. Phys. Chem. C* **2018**, 122, 5553–5565.

97. Wang, X.; Shi, H.; Szanyi, J., Controlling selectives in CO_2 reduction through mechanistic understanding. *Nat. Commun.* **2017,** 8, 513-519.

98. Baltrusaitis, J.; Schuttlefield, J.; Zeitler, E.; Grassian, V.H., Carbon dioxide adsorption on oxide nanoparticle surfaces. *Chem. Eng. J.* **2011**, 170, 471–481.

99. Raskó, J.; Kecskés, T.; Kiss, J. Adsorption and reaction of formaldehyde on TiO_2-supported Rh catalysts studied by FTIR and mass spectrometry. *J. Catal*. **2004**, 226, 183-191.

100. Simanouchi, T., Tables of Molecular Vibrational Frequeces Consolidated, Vol. 1, National Bureau of Standards, **1972**

101. Ichikawa, M.; Fukushima, T., Infrared studies of metal additive effects on carbon monoxide chemisorption modes on silicon dioxide-supported rhodium-manganese, -titanium and iron catalysts. *J. Phys. Chem.* **1985**, 89, 1564-1567.

102. Stevenson, S.A.; Lisistsyn, A.; Knözinger, H., Adsorption of carbon monoxide on manganese-promoted rhodium/silica catalysts as studied by infrared spectroscopy. *J. Phys. Chem.* **1990**, 94, 1576-1581.

103. Chuang, S.S.C.; Stevens, R.W.; Khatri, R., Mechanism of C_{2+} oxygenate synthesis on Rh catalysts. *Top. Catal*. **2005**, 32, 225-232.

104. Sápi, A.; Kashaboina, U.; Baán, K.; Perez Gomez, J.; Szenti, I.; Halasi, Gy.; Kiss, J.; Nagy, B.; Varga, T.; Kukovecz, Á.; Kónya, Z., Synergetic of Pt nanoparticles and H-ZSM-5 zeolites for efficient CO_2 activation: Role of interfacial sites in high activity. *Frontiers in Materials*, **2019**, 127, 6p

105. Kattel, S.; Yan, B.; Chen, J.G.; Liu, P. CO_2 hydrogenation on Pt, Pt/SiO_2 and Pt/TiO_2: Importance of synergy between Pt and oxide support. *J. Catal*. **2016,** 343, 115-120.

106. Fisher, A.I.; Bell, A.T., A Comparative Study of CO and CO_2 Hydrogenation over Rh/SiO_2. *J. Catal*. **1996**, *162*, 54–65.

107. Byron, S.R.J.; Muruganandam, I.; Murthy, S.S., A review of the water gas shift reaction kinetics, *Int. J. Chem. React. Eng*. **2010**, 8.

108. Gokhale, A.A.; Dumesic, J.A.; Mavrikakis, M.M., On the mechanism of low temperature water gas shift reaction on copper. *J. Amer. Chem. Soc*, **2008**, 130, 1402–1414.

109. Soria, M.A.; Perez, P.; Carabineiro, S.A.C.; Hodar, F.J.M.; Mendes, A.; Madeira, L.M. Effect of the preparation method on the catalytic activity and stability of Au/Fe_2O_3 catalysts in the low-temperature water–gas shift reaction. *Appl.Catal. A: General* **2014**, 470, 45-55.

110. Lloyd, L.; Ridler, D.E.; Twigg, M.V., 'The Water-Gas Shift Reaction', in "Catalyst Handbook", M. V. Twigg (Ed), 2nd edition, Manson Publishing Ltd., Frome, Chapter **1996**, 6, p. 283

111. Ladebeck, J.R.; Wagner, J.P., Catalyst development for water-gas shift. *Handbook of Fuel Cell-Fundamentals, Technology and Applications: Edited by Wolf Vielstich, Arnold Lamm, Hubert A. Gasteiger,* **2003**, 3, 190-201.

112. Li, Y.; Fu, Q.; Flytzani-Stephanopoulos, M., Low-temperature water-gas shift reaction over Cu- and Ni-loaded cerium oxide catalysts. *Appl. Catal. B: Envir.* **2000**, 27, 179-191.

113. Li, J.; Yoon, H.; Oh, H.T.; Washman, E.D., $SrCe_{0.7}Zr_{0.2}Eu_{0.1}O_3$-based hydrogen transport water gas shift reactor. *Int. J. Hydrogen Energy* **2012**, 37, 16006- 16012.

114. Grabow, L.C.; Gokhale, A.A.; Evans, S.T.; Dumesic, A.; Mavrikakis, M., Mechanism of the water gas shift reaction on Pt: First Principles, Experiments, and microkinetic modeling. *J. Phys. Chem. C*. **2008**, 112, 4608-4617.

115. Ovesen, C.V.; Clausen, B.S.; Hammershoi, B.S.; Steffensen, G.; Askgaard, T.; Chorkendorff, I.; Norskov, J.K.; Rasmussen, P.B.; Stolze, P.; Taylor P.A., Microkinetic analysis of the water gas reaction under industrial conditions. *J. of Catalysis*, **1996**, 158, 170–180.

116. Kölbel, H.; Bhasttocharga, K.K., Synthese hochschmelzender Paraffine an Ruthenium-Kontakten. *Just.Leibigs Ann. Chem*. **1958**, 618, 67-71.

117. Niwa, M.; Lunsford, L.H., The catalityc reactions of CO and H_2O over supported rhodium *J. Catal*. **1982**, 75, 302-313.

118. Solymosi, F.; Erdőhelyi, A.; Tombácz, I., Methane synthesis in the H_2O +CO reaction over titania supported Rh and Rh-Pt catalysts. *Appl. Catal.* **1985,** 14, 65-67.

119. Diagne, C.; Idriss, H.; Kiennemann, A., Hydrogen production by ethanol reforming over Rh/CeO_2-ZrO_2 catalysts. *Catal. Commun.* **2002,** 3, 565-571.

120. Aupretre, F.; Descorme, C.; Duprez, D., Bio-ethanol catalytic steam reforming over supported metal catalysts. *Catal. Commun.* **2002,** 3, 263-267.

121. Liguras, D. K.; Kondarides, D.J.; Verykios, X.E., Production of hydrogen for fuel cells by steam-reforming of ethanol over supported noble metal catalysts. *Appl. Catal. B: Environ.* **2003,** 43, 345-354.

122. Raskó, J.; Hancz, A.; Erdőhelyi, A, Surface species and gas phase products in steam reforming of ethanol on TiO_2 and Rh/TiO_2. *Appl. Catal. A: General* **2004,** 269, 13-25.

123. Erdőhelyi, A.; Raskó, J.; Kecskés, T.; Tóth, M.; Dömök, M.; Baán, K, Hydrogen formation in ethanol steam reforming on supported noblemetal catalysts. *Catal. Today* **2006,** 116, 367-376.

124. Ferencz, Zs.; Erdőhelyi, A.; Baán, K.; Oszkó, A.; Óvári, L.; Kónya, Z.; Papp, C.; Steinrück, H.-P.; Kiss, J, Effects of Support and Rh Additive on Co-Based Catalysts in the Ethanol Steam Reforming Reaction. *ACS Catal.* **2014,** 4, 1205-1218.

125. Idriss, H.; Seebauer, E. G., Reactions of ethanol over metal oxide. *J. Mol. Catal.* A **2000,** 152, 201-212.

126. Nadeem, M.A.; M. Murdoch, M.; Waterhouse, G.I.N.; Metson, J.B.; Keane, M.A.; Llorca, J.; Idriss, H., Photoreaction of ethanol on Au/TiO_2 anatase: Comparing the micro to nanoparticlesize activities of the support for hydrogen production. *J. Photochem. Photobiol. A: Chem.* **2010,** 216, 250-255.

127. Papageorgopoulos, D. C.; Ge, Q.; King, D. A. Synchronous Thermal Desorption and Decomposition of Ethanol on Rh{111}. J. Phys. Chem. **1995,** 99 (49), 17645–17649.

128. Houtman, C. J.; Barteau, M. A. Divergent Pathways of Acetaldehyde and Ethanol Decarbonylation on the Rh(111) Surface. J. Catal. **1991,** 130 (2), 528–546.

129. de Lima, S.M.; da Cruz, I.O.; Jacobs, G.; Davis, B.H.; Mattos, L.V.; Noronha, F.B., Steam reforming, partal oxidation, and oxidative steam reforming of ethanol over Pt/$CeZrO_2$ catalyst. *J. Catal*. **2008,** 257, 356-368

130. Tóth, M.; Varga, E.; Baán, K.; Oszkó, A.; Kiss, J.; Erdőhelyi, A, Partial oxidation of ethanol on supported Rh catalysts: Effect of the oxide support. *J. Mol. Catal. A: Chemical* **2016,** 411, 377-387.

131. Solymosi, F.; Erdőhelyi, A.; Kocsis, M., Surface interaction between H_2 and CO_2 on Rh/Al_2O_3 studied by adsorption and infrared spectroscopic measurements. *J. Catal.* **1980,** 65, 428-436

132. Di Cosimo, J.I.; Diez, V.K.; Xu, M.; Iglesia, E.; Apesteguia, C.R., Structure and Surface and Catalytic Properties of Mg-Al Basic Oxides. *J. Catal.* **1998,** 178, 499-510.